Shear band formation in porous thin-walled tubes subjected to dynamic torsion

A. R. Vishnu, J. C. Nieto-Fuentes, J. A. Rodríguez-Martínez*

Department of Continuum Mechanics and Structural Analysis. University Carlos III of Madrid. Avda. de la Universidad, 30. 28911 Leganés, Madrid, Spain

Abstract

In this paper, we have performed 3D finite element calculations of thin-walled tubes subjected to dynamic twisting to investigate the effect of porous microstructure on the formation of shear localization bands under simple shear conditions. For that purpose, we have incorporated into the finite element model the porous microstructures of four different additive manufactured metals –aluminium alloy AlSi10Mg, stainless steel 316L, titanium alloy Ti6Al4V and Inconel 718– for which the void volume fraction varies from ≈ 0.001 % to ≈ 2 %, and the voids size between ≈ 6 μm and ≈ 110 μm (Marvi-Mashhadi et al., 2021). For each microstructure, we have created up to 10 realizations varying the spatial location of the voids and the distribution of voids size. The matrix material is elastic/plastic, with yielding defined by the von Mises yield criterion and associated flow rule. The yield stress evolution is considered to be dependent on strain, strain rate and temperature, with parameters corresponding to Titanium and HY-100 Steel, taken from Molinari (1997) and Batra and Kim (1990), respectively. Moreover, we have assumed the deformation process to be adiabatic. The calculations have been performed for shear strain rates ranging from 100 s^{-1} to 10000 s^{-1}. To the authors' knowledge, this is the first study ever that simulates dynamic torsion testing of porous materials with actual representation of voids, providing new results which bring to light the influence of porosity on dynamic shear banding under simple shearing. Namely, the numerical calculations have shown that both the location of the shear band and the critical strain leading to the shear band formation depend on the spatial and size distribution of the voids in the specimen, evidencing the influence of material defects on the localization pattern. Notably, the shear band nucleation strain decreases with both the void volume fraction in the specimen and the size of the voids, the size of the largest pore being the main microstructural feature controlling the loss of load carrying capacity of the specimen. In addition, we have carried out a parametric analysis varying the temperature and strain rate sensitivities of the material, and the loading rate. For the strain rates investigated, increasing the loading speed leads to a mild decrease of the shear strain leading to shear band formation, while the strain rate sensitivity is shown to stabilize material behavior and delay localization. Moreover, the numerical results have made apparent that for the materials considered, thermal softening is essential to trigger the shear

*Corresponding author. E-mail address. jarmarti@ing.uc3m.es

band formation, so that the porous microstructure alone does not lead to shear localization.

Keywords:
Shear bands, Dynamic torsion, Porous microstructure, Void shearing, Finite element calculations

1. Introduction

The formation of shear bands in metals subjected to high strain rates leads to material failure during high-speed machining operations (Molinari et al., 2002; Burns and Davies, 2002; Ye et al., 2013), blast and explosions (Wiehahn et al., 2000), ballistic impacts (Børvik et al., 2001; Zou et al., 2011) and high velocity metalworking processes (Gaudillière et al., 2010; Schmitz et al., 2020), just to name a few relevant engineering applications.

Several experimental techniques have been developed over the years to study in a controlled laboratory environment the mechanisms triggering dynamic shear bands formation (see Chapter 2 of Dodd and Bai (2012)). For instance, Duffy and co-workers (Marchand and Duffy, 1988; Hartley et al., 1987; Duffy and Chi, 1992; Cho et al., 1990) used a torsional split Hopkinson bar apparatus to twist thin-walled tubes made of various grades of steel at nominal strain rates in the range of 10^3 s^{-1} to $5 \cdot 10^3$ s^{-1}. A single shear band was formed in the gauge section of the specimen prior to material fracture. Consistent with the postulate of Zener and Hollomon (1944), Marchand and Duffy (1988) observed that the shear band occurred when the thermal softening due to adiabatic heating overtook the strain hardening of the material, and identified three stages in the process of shear localization. Firstly, the plastic deformation in the gauge section of the specimen was homogeneous during the initial hardening of the material. Secondly, the strain field became inhomogeneous with progressive localization of plastic deformation upon loading. Finally, the third stage was recognized by the localized plastic strains conforming to a narrow band leading to the final specimen collapse. Dynamic torsion experiments were also performed by Giovanola (1988a) to characterize the energy dissipation and temperature increase during dynamic shear banding in VAR 4340 steel at nominal strain rates ranging between 10^3 s^{-1} and $8 \cdot 10^3$ s^{-1}, and by Ramesh (1994) to determine the lower strain rate $\left(\approx 260 \text{ s}^{-1}\right)$ for which shear bands form in a tungsten heavy alloy. Moreover, Bai et al. (1994) modified the torsional Hopkinson bar setup to interrupt the process of shear localization at different stages in Ti6A14V samples tested at ≈ 300 s^{-1}, and thus noticed the progressive nucleation of voids within the band which eventually coalesced leading to elongated cavities and micro-cracks which triggered material fracture. This work made apparent that, on top of thermal effects, microstructural evolutions also contribute to the formation of shear bands (see also Cho et al. (1993) and Mgbokwere et al. (1994)). Elongated and coalesced voids were also noticed in dynamic shear bands formed in torsional test specimens made of 4340 steel (Giovanola, 1988b). The fractographic analysis of the post-portem samples demonstrated that softening due to the nucleation and growth of microvoids was responsible for the late stage of the localization process and the final fracture of the specimens. Moreover, Da Silva and Ramesh (1997) performed dynamic torsion of thin tubes made of Ti6Al4V. Fully dense and porous specimens ($\approx 7.6\%$ of void volume fraction) were tested at a nominal strain rate of $8 \cdot 10^2$ s^{-1}. The experimental results showed that shear bands form earlier in the porous material, reinforcing the idea of Dodd and Atkins (1983) that for materials containing voids on a microscopic level, the geometrical softening between the voids promotes early shear localization. Note that deformed voids were also observed in dynamic shear bands formed in specimens subjected to high strain rate loading other than torsion, e.g., in thick-walled cylinders subjected to rapid radial collapse in which multiple shear bands are incepted at large strains (Xue et al., 2002; Odeshi et al., 2006; Yang et al., 2011; Lovinger et al., 2015).

Finite element analysis of specimens subjected to dynamic torsion provided additional insights into the mechanics of shear banding. Johnson (1981) carried out calculations of copper thin-walled tubes tested at ≈ 300 s^{-1}. The mechanical behavior of the material was considered to be a function of strain, strain rate and temperature. The inception and development of the shear bands was shown to be dependent on the temperature sensitivity of the material, so that increasing thermal softening favored early localization and increased the speed of development of the band. Feng and Bassim (1999) performed coupled thermo-mechanical analysis –considering conversion of plastic work into heat and thermal conductivity– of torsional test specimens made of 4340 steel and modeled with a thermo-viscoplastic constitutive relation. The imposed nominal strain rate was 1000 s^{-1}. It was shown that material defects are preferential sites for the formation of shear bands, with the thermal conduction providing the shear band with a finite width (a similar conclusion was reached by Dodd and Bai (1985) and Batra and Kim (1991), among others). Moreover, it was stated that the rate of development of the shear band results from the competition of the stabilizing/destabilizing effects of strain hardening and thermal softening on the material flow stress. The speed of propagation of the shear band in dynamic torsional tests was determined by Batra and Zhang (1994) using finite element simulations of 4340 steel samples twisted at various strain rates ranging from 1000 s^{-1} to 25000 s^{-1}. It was shown that when the tube is loaded at a nominal strain rate of 25000 s^{-1}, the band speed varies from 180 m/s at the site of the initiation to approximately 1000 m/s at the nearly diametrically opposite point. Moreover, Batra and Kim (1990) pointed out the sensitivity of the numerical results for the temperature and strain fields near the band to the viscoplasic flow rule used to model the material behavior. An incomplete list of additional papers performing finite element calculations of shear bands formation in torsional test samples is

(Johnson et al., 1983; Batra and Kim, 1992; Bonnet-Lebouvier et al., 2002; Chichili et al., 2004; Glema et al., 2008; Dolinski et al., 2010; Arriaga and Waisman, 2017). All of these papers consider the material to be fully dense.

In fact, the number of works simulating shear localization in porous specimens subjected to dynamic torsion is scarce. Kobayashi and Dodd (1989) investigated the formation of adiabatic shear bands in low carbon steel and pure titanium accounting for the effect of void nucleation and growth. It was shown that geometrical imperfections such as voids play an important role in locating shear bands, although the thermal softening effect was the critical factor in the development of the localization. Łodygowski and Perzyna (1997b) modeled adiabatic shear band localized fracture in thin-walled tubes subjected to dynamic twisting using a thermo-viscoplastic model which considers micromechanical damage –which accounts for void nucleation, growth and void interaction– as an internal state variable (see also Perzyna (1994) and Łodygowski and Perzyna (1997a)). The predictions for the width of the shear band, and the temperature rise within the shear localization zone, were shown to be in quantitative agreement with the experimental evidence reported by Hartley et al. (1987) and Marchand and Duffy (1988). Moreover, Kubair et al. (2015) performed 1D finite difference simulations of multiple shear bands formation in a metallic specimen with preexisting voids and subjected to boundary conditions consistent with the torsional test specimen. The mechanical behavior of the material was described with the constitutive model developed by Nahshon and Hutchinson (2008), who developed a phenomenological extension of the flow potential of Gurson (1977) to account for void evolution under shear deformation. It was shown that porosity promotes early shear localization. A few authors have performed numerical simulations of shear banding in porous materials for high loading rate problems other than dynamic twisting of thin-walled tubes (i.e., stress states other than simple shear). For instance, the constitutive model of Nahshon and Hutchinson (2008) was used by Pascon and Waisman (2021) to perform 2D finite element calculations of two benchmark problems: a rectangular plate subjected to axial extension and a notched bar under tensile loading. Consistent with the results of Kubair et al. (2015), the void shearing mechanism was found to accelerate material damage, leading to early shear band formation. Moreover, Dorothy and Longère (2019) performed 3D finite element simulations of shear band formation in hat-shape specimens impacted at 30 m/s. The mechanical behavior of the material was modeled using a continuum damage mechanics constitutive model with a phenomenological potential which accounts for voids growth and degrades the material properties as plastic deformation evolves. The calculations showed that voids softening accelerates the propagation of shear bands.

However, while the results reported in the works cited in the previous paragraph are consistent with the experimental evidence, indicating that voids softening promotes shear localization, it has to be noted that the constitutive models employed in these studies are based on *ad-hoc* definitions of the void shearing/softening mechanisms (i.e., the mathematical construction of the constitutive models is such that porosity grows under shear loading). Note also that in the constitutive theories employed by Kobayashi and Dodd (1989), Łodygowski and Perzyna (1997b), Dorothy and Longère (2019) and Pascon and Waisman (2021), the void shearing induced softening is represented by a damage function that depends only on the void volume fraction and on the state of stress, and does not account for the effect of the spatial and size distribution of voids, thereby disregarding the inherent heterogeneity of the porous microstructure in metals and alloys. This *limitation* has been recently overcome by Vishnu et al. (2022) in 3D finite element calculations of electro-magnetically collapsing thick-walled cylinders containing explicitly resolved voids. The distribution of voids sizes was taken from additive manufactured metals with void volume fraction less than 2%, and pore sizes varying from ≈ 6 μm to ≈ 110 μm. The voids were taken to be randomly distributed in the finite element model. The simulations provided insights into the role of actual porous microstructure on the collective behavior and spacing of multiple shear bands. Namely, it was shown that the number of shear bands increases as the number of voids increases, and the shear bands are incepted earlier and develop faster as the size of the pores increases.

In this paper, we adapt the methodology of Vishnu et al. (2022) to simulate shear localization in thin-walled tubes subjected to dynamic twisting. In comparison with the collapse of thick-walled cylinders, in which multiple shear bands are incepted, the torsion test shows the advantage that a single principal shear band is formed (also referred to as main shear band along this paper), and the stress of state is of simple shear during the whole loading process, which facilitates the interpretation of results. We have performed calculations at different strain rates ranging from 110 s^{-1} to 10000 s^{-1}, for void volume fractions varying from $\approx 0.001\%$ to $\approx 2\%$, and void sizes varying between ≈ 6 μm to ≈ 100 μm. A key point of the methodology is that for a given void volume fraction and distribution of void sizes, we have created up to 10 microstructural realizations with different random spatial and size distribution of voids, showing the effect of the stochastic location of the voids on the shear band formation. To the authors' knowledge, this is the first paper ever which simulates the torsion test in porous materials with actual representation of voids. The calculations carried out in this work provide quantitative analysis on the effect of void volume fraction and voids size distribution on the critical strain leading to shear band inception.

2. Constitutive framework

The mechanical behavior of the material is modeled using isotropic linear elasticity and von Mises (1928) plasticity. The rate of deformation tensor $\boldsymbol{d}$ is taken to be the addition of elastic ($\boldsymbol{d}^e$) and plastic ($\boldsymbol{d}^p$) components:

$$\boldsymbol{d} = \boldsymbol{d}^e + \boldsymbol{d}^p \tag{1}$$

The elastic deformation rate is related to the rate of the stress:

$$\dot{\boldsymbol{\sigma}} = \boldsymbol{C} : \boldsymbol{d}^e \tag{2}$$

where $\dot{\boldsymbol{\sigma}}$ is an objective derivative of the Cauchy stress tensor ($\boldsymbol{\sigma}$) –which corresponds to the Jaumann rate in ABAQUS/Standard (2019)– and $\boldsymbol{C}$ is the tensor of isotropic elastic moduli:

$$\boldsymbol{C} = 2G\tilde{\mathbf{I}} + K\mathbf{1} \otimes \mathbf{1} \tag{3}$$

where G is the elastic shear modulus, K is the bulk modulus, $\mathbf{1}$ is the second-order unit tensor and $\tilde{\mathbf{I}}$ is the fourth-order deviatoric unit tensor.

The plastic deformation rate is defined as:

$$\boldsymbol{d}^p = \dot{\lambda} \frac{\partial f}{\partial \boldsymbol{\sigma}} \tag{4}$$

where $\dot{\lambda}$ is the plastic flow proportionality factor and $f = \bar{\sigma} - \sigma_Y \leq 0$ is the yield condition, with $\bar{\sigma} = \sqrt{\frac{3}{2}\boldsymbol{s} : \boldsymbol{s}}$ being the von Mises effective stress, where $\boldsymbol{s} = \boldsymbol{\sigma} - \sigma_h : \mathbf{1}$ and $\sigma_h = \frac{1}{3}\boldsymbol{\sigma} : \mathbf{1}$ are the deviatoric component of the Cauchy stress tensor and the hydrostatic stress, respectively. Moreover, σ_Y is the yield stress of the material which is a function of the effective plastic strain ($\bar{\varepsilon}^p$), the effective plastic strain rate ($\dot{\bar{\varepsilon}}^p$) and the temperature ($T$):

$$\sigma_Y = \sigma_0(\bar{\varepsilon}^p + \varepsilon_{ref})^n \left(\frac{\dot{\bar{\varepsilon}}^p}{\dot{\varepsilon}_{ref}}\right)^m \left(\frac{T}{T_{ref}}\right)^\nu \tag{5}$$

where $\bar{\varepsilon}^p = \int_0^t \dot{\bar{\varepsilon}}^p(\tau)d\tau$ and $\dot{\bar{\varepsilon}}^p = \sqrt{\frac{2}{3}\boldsymbol{d}^p : \boldsymbol{d}^p}$. The parameter σ_0 is the initial yield stress, and n, m and ν are the strain hardening, strain rate sensitivity and temperature sensitivity exponents, respectively. Moreover, ε_{ref}, $\dot{\varepsilon}_{ref}$ and T_{ref} are the reference strain, strain rate and temperature.

We have assumed the deformation process to be adiabatic, so that the energy equation takes the form:

$$\rho C_p \dot{T} = \beta \bar{\sigma} \dot{\bar{\varepsilon}}^p \tag{6}$$

where ρ is the current material density, C_p the specific heat and β the Taylor-Quinney coefficient.

The baseline constitutive parameters used in the calculations presented in Sections 4, 5, 6 and 7 correspond to Titanium and HY-100 Steel, and they are taken from Molinari (1997) and Batra and Kim (1990) respectively, see Table 1. Note that HY-100 Steel was used in the dynamic torsion experiments of Marchand and Duffy (1988).

Symbol	Property and units	Titanium	HY-100 Steel
ρ_0	Initial density (kg/m^3)	4510	7860
G	Elastic shear modulus (GPa), Eq. (3)	43.28	76
K	Bulk modulus (GPa), Eq. (3)	120.83	164.4
C_p	Specic heat (J/Kg K), Eq. (6)	528	473
β	Taylor-Quinney coefficient, Eq. (6)	0.9	0.9
σ_0	Initial yield stress parameter (MPa), Eq. (5)	1171.45	1201.88
n	Strain hardening exponent, Eq. (5)	0.15	0.107
m	Strain rate sensitivity exponent, Eq. (5)	0.033	0.0117
ν	Temperature sensitivity exponent, Eq. (5)	-1.7	-0.75
ε_{ref}	Reference strain, Eq. (5)	5.77×10^{-3}	0
$\dot{\varepsilon}_{ref}$	Reference strain rate (s^{-1}), Eq. (5)	0.001	0.0001
T_{ref}	Reference temperature (K) , Eq. (5)	293	293

Table 1: Numerical values of initial density, elastic constants, physical constants and parameters of the yield stress corresponding to Titanium and HY-100 Steel. Data for Titanium and HY-100 Steel after Molinari (1997) and Batra and Kim (1990), respectively.

3. Finite element model

The finite element model is primarily based on the experimental configuration of Marchand and Duffy (1988). The torsion specimen is a short and thin tube located between two hexagonal flanges which can be fitted into matching hexagonal sockets in the Kolsky bars set up (see Fig. 1 therein). However, for the sake of simplicity, we have modeled only the gauge section (thin tubular section), as in Batra and Zhang (1994). The tubular specimen has an internal diameter of 9.5 mm, wall thickness of 0.38 mm and height of 2.5 mm, denoted by d, w and h, respectively. Material points are referred to using cylindrical coordinates (R, Θ, Z). The origin of the coordinate system is located at the center of mass of the tube (see Fig. 1). The unit vectors along the coordinates are represented by $(\hat{\boldsymbol{e}}_R, \hat{\boldsymbol{e}}_\Theta, \hat{\boldsymbol{e}}_Z)$.

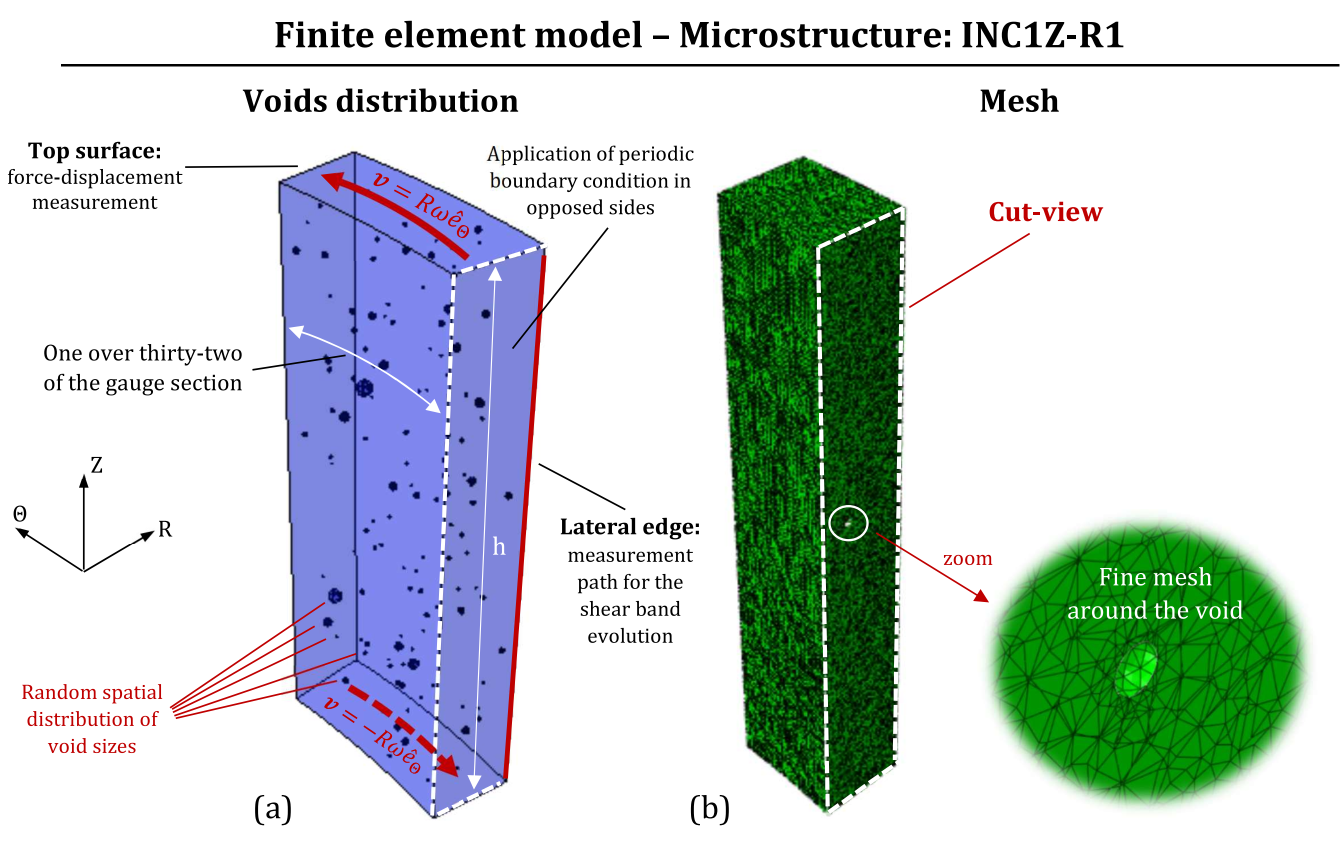

Figure 1: Finite element model developed in ABAQUS/Standard (2019) to investigate shear banding in thin-walled tubes subjected to dynamic torsion. The model consists of one over thirty-two of the gauge section of the specimen with periodic boundary conditions. (a) Spatial and size distribution of spherical voids corresponding to microstructure INC1Z and realization R1. The twisting velocity boundary condition is applied on upper and bottom sides of the gauge section $\boldsymbol{v}(R, \Theta, \frac{h}{2}, t) = \pm R\omega\hat{\boldsymbol{e}}_\Theta$. (b) Discretization using ten-node quadratic tetrahedral elements. Detail of the mesh size around the voids.

The novelty of the dynamic torsion calculations presented in this paper is that we have included explicitly resolved spherical voids in the finite element model to study the effect of porosity on shear band formation. For that purpose, we have followed the methodology developed by Marvi-Mashhadi et al. (2021) and Vishnu et al.

(2022), importing into ABAQUS the representative porous microstructures of four additive manufactured metals: aluminium alloy AlSi10Mg, stainless steel 316L, titanium alloy Ti6Al4V and Inconel 718 (referred to as Al3XY, SS5XY, Ti0.5XY and INC1Z, respectively). The main features of the porous microstructures investigated are reported in Table 2. Notice that the four microstructures show large differences in void volume fraction (f_0), voids density ($\overline{\text{Voids}}$) and maximum voids diameter (d_{max}), which facilitates obtaining a clear picture of the effect of porosity on shear bands formation under torsion loading. The distributions of void sizes have been fitted to a Log-normal statistical distribution with mean (μ) and standard deviation (dev) given in Table 2. For each of the four porous microstructures considered, we have created up to ten realizations of void size and position distribution which fulfill the same Log-normal statistical function, in order to take into account the scatter in the finite element results caused by the random spatial distribution of pores (namely, ten realizations for INC1Z –see Section 4– and three for Al3XY, SS5XY and Ti0.5XY). These realizations will be referred to as R1, R2, ... , R10. For a detailed description of the procedure devised for the generation of the porous microstructures, the reader is referred to Sections 2 and 3 of Marvi-Mashhadi et al. (2021), and Sections 3 and 4 of Vishnu et al. (2022). Note that in this paper the additive manufactured materials are solely employed to obtain representative porosity distributions to be used in the simulations of Sections 4, 5, 6 and 7. The mechanical behavior of the twisted thin tubes is described by the constitutive model presented in Section 2 and the parameters of Table 1. The constitutive framework has been implemented using the linear elasticity and von Mises plasticity models available in ABAQUS/Standard (2019), while the yield stress evolution described by equation (5) has been coded using a UHARD subroutine.

	Al3XY	SS5XY	Ti0.5XY	INC1Z
f_0 (%)	2.17	0.0025	0.0013	0.1363
$\overline{\text{Voids}}$ ($num./mm^3$)	5985	17	5	147
d_{max} (μm)	110.53	41.40	26.93	78.93
d_{min} (μm)	8.00	7.40	8.27	7.45
μ (μm)	15.98	11.21	17.30	16.58
dev (μm)	4.57	5.13	5.03	7.71

Table 2: Main features of the porous microstructures investigated: initial void volume fraction (f_0), number of voids per mm^3 ($\overline{\text{Voids}}$), maximum voids diameter (d_{max}), minimum voids diameter (d_{min}), and mean (μ) and standard deviation (dev) of fitted Log-normal distribution. Results taken from Marvi-Mashhadi et al. (2021).

A very fine mesh is necessary to capture the geometry of the pores in the specimen, so that we have modeled only one over thirty-two of the gauge section along the circumferential direction, imposing periodic boundary conditions which ensure the continuity in displacements and thereby the continuity in stress and strain fields in the circumferential direction, see Fig. 1. A fine mesh is also required to model the localization process, with elements' size of the order of the width of the shear band (see discussion below). We assume that the reduced numerical model enables to include sufficient number of pores which are representative of the actual microstructures investigated, see Table 3.

	Al3XY			SS5XY			Ti0.5XY			INC1Z									
	R1	R2	R3	R1	R2	R3	R1	R2	R3	R1	R2	R3	R4	R5	R6	R7	R8	R9	R10
f_0 (%)	1.548	1.391	1.426	0.010	0.006	0.003	0.002	0.004	0.001	0.075	0.039	0.059	0.073	0.046	0.114	0.060	0.043	0.046	0.132
$\overline{\text{Voids}}$ ($num./mm^3$)	5656	5490	5609	15	21	19	6	4	3	133	129	142	154	126	146	130	151	140	146
Voids *(num.)*	5212	5059	5169	14	19	18	6	4	3	123	119	131	142	116	135	120	139	129	135
d_{max} (μm)	76.87	69.00	76.70	30.34	30.27	26.33	28.20	33.60	21.87	62.36	60.29	70.30	52.84	38.83	86.33	44.78	60.23	42.30	86.77

Table 3: Initial void volume fraction (f_0), number of voids per mm^3 ($\overline{\text{Voids}}$), number of voids (Voids) and maximum void diameter (d_{max}) in the finite element models corresponding to each realization generated for the microstructures investigated.

The twisting load is applied using the following boundary conditions:

$$\boldsymbol{v}(R, \Theta, \tfrac{h}{2}, t) = R\omega\hat{\boldsymbol{e}}_\Theta; \quad \boldsymbol{v}(R, \Theta, -\tfrac{h}{2}, t) = -R\omega\hat{\boldsymbol{e}}_\Theta \tag{7}$$

where $\boldsymbol{v}$ is the velocity, t is the time and ω is the applied angular speed, see Fig. 1. The inner and outer surfaces of the specimen are traction free, i.e., $\boldsymbol{\sigma} \cdot \hat{\boldsymbol{e}}_R = \mathbf{0}$. The nominal shear strain rates investigated in this paper vary within the range $100 \text{ s}^{-1} \leq \dot{\gamma}_0 \leq 10000 \text{ s}^{-1}$, where $\dot{\gamma}_0 = \dfrac{2R\omega}{h}$.

The following initial conditions are applied to the specimen:

$$\boldsymbol{v}(R, \Theta, Z, 0) = \frac{2R\omega}{h} Z\hat{\boldsymbol{e}}_\Theta; \qquad T(R, \Theta, Z, 0) = T_{ref} \tag{8}$$

Note that the velocity initial condition allows to minimize the propagation of stress waves within the specimen caused by the abrupt motion of the thin tube at $t = 0$. Otherwise, the waves generated due to the application of the velocity boundary conditions could lead to instantaneous plastic localization (Needleman, 1991; Xue et al., 2008).

The calculations have been carried out using the dynamic implicit solver of ABAQUS/Standard (2019). The specimen has been discretized with modified ten-node quadratic tetrahedral elements (C3D10M in ABAQUS notation), as they are particularly robust for large deformation analysis and contact problems. The edges of the specimen have been seeded with elements of size ≈ 20 μm to 30 μm, and the meridian of the smallest void has meshed with 4 to 5 elements (Marvi-Mashhadi et al., 2021). Moreover, as the number of voids increases, the mesh size increases. Namely, the microstructures Al3XY, SS5XY, Ti0.5XY and INC1XY contain $\approx$ 3.5, 0.65, 0.6 and 0.8 million elements, respectively. We have also checked that there are at least 2-3 elements within the main shear band that develops in the samples at large strains. Moreover, the frictionless and hard pressure-overclosure contact constraint available in ABAQUS/Standard (2019) has been used to define the contact between the void surfaces during deformation. The calculations have been performed using a workstation AMD Milan 7453 @ 2.75 GHz with 56 cores. The computational cost of each simulation shown in this paper ranged between 2 and 12 days, depending on the microstructure considered, using simultaneously all the cores of the workstation.

The evolution of void volume fraction in the specimen during loading –presented in Sections 4.1 and 5.1– is obtained with the following two-steps methodology:

- The volume of the matrix material at each time step (MMV) is the summation of the individual elemental volumes ($EVOL$):

$$MMV = \sum_{n=1}^{n_{elem}} EVOL_n \tag{9}$$

  where n_{elem} is the total number of elements in the model.

- The nodal coordinates of the outer surfaces of the thin tube at each time step are exported to MATLAB®, so that the *alphaShape* function computes the total volume of the specimen (V).

Finally, the void volume fraction at each time step (f), is computed as:

$$f = \frac{V - MMV}{V} \tag{10}$$

4. Salient results

The finite element simulations reported in this section correspond to the four porous microstructures and all the realizations reported in Tables 2 and 3. Results are shown for both Titanium and HY-100 Steel, see Table 1. The nominal shear strain rate is $\dot{\gamma}_0 = 1000$ s^{-1} (strain rate routinely used in dynamic torsion experiments, see Section

1). In Section 4.1, we compare calculations performed with fully dense material (i.e., $f_0 = 0$) and with porous microstructure INC1Z and realization R3. The results illustrate the effect of actual porosity on the formation and development of adiabatic shear bands under dynamic torsion. The microstructure INC1Z is selected because it shows intermediate values of the void volume fraction, of the number of voids and of the maximum diameter of the voids, see Table 2, so that the outcomes of the analysis are considered to be representative of the porosity distributions investigated in this work. Section 4.2 compares the results obtained with the ten realizations of microstructure INC1Z (R1, R2, ... , R10), see Table 3. It is shown that the topology of the porous microstructure and the distribution of voids size affect the critical strain triggering the formation of the shear band, and the specific location where the shear band nucleates. In Section 4.3, the comparison of results obtained with microstructures Al3XY, SS5XY and Ti0.5XY provides individualized correlations between the critical strain at which the shear band is formed and the main features of the porous microstructure (void volume fraction and maximum diameter of the voids).

4.1. The comparison between porous and fully dense materials

Fig. 2 shows contours of effective plastic strain $\bar{\varepsilon}$ for microstructure INC1Z-R3 and different loading times. The color coding of the isocontours is such that effective plastic strains ranging from 0.1 to 0.4 correlate with a color scale that goes from blue to red. Effective plastic strains below 0.1 remain blue, and above 0.4 remain red. The semi-transparent view of the specimen in pictures (a)-(b)-(c)-(d)-(e)-(f) shows the evolution of the porous microstructure, and the cut-view in pictures (e)-(f)-(g) illustrates the development of the shear band plane. The material parameters correspond to Titanium (see Table 1).

Semi-transparent picture (a) shows the specimen at $t = 0$ μs, and the velocity boundary condition for application of the twisting load. The microstructure contains pores of different sizes randomly distributed in the sample. Semi-transparent picture (b) corresponds to $t = 100$ μs. For this loading time, the strain in the specimen is largely homogeneous because the shear force in the sample is increasing, see white marker in Fig. 3 (green dashed curve corresponds to microstructure INC1Z-R3). Semi-transparent picture (c) illustrates the nucleation of the shear localization (which appears as a light blue plane near the mid section of the sample), as for this loading time $t = 200$ μs the force is maximum, black marker in Fig. 3. Note that localization of plastic deformation also occurs near large pores located in different parts of the sample (light blue spots), which act as strain concentrators. Semi-transparent pictures (d) and (e) show the development of the shear band (which turns into a light green plane), which corresponds to the gradual decrease of the force in the specimen, which is indicated with yellow markers in Fig. 3. The fully developed shear band is shown in semi-transparent picture (f), which is taken for a loading time immediately preceding the drastic drop of the force representing the loss of load carrying capacity of the specimen, see blue marker in Fig. 3. The shear band corresponds to the red plane, which contains the largest pore of the microstructure, this being the trigger for the localization. Notice that the void has lost the spherical shape, becoming ellipsoidal, elongated along the circumferential direction of the sample, after twisting and rotating due to the applied torsional loading. However, the void volume fraction in the specimen virtually remains constant during loading, with a slight increase when the shear band is formed, see Fig. 3 (the black dashed curve represents the evolution of the void volume fraction with the angular displacement). This is consistent with the fact that the volume of the material remains constant under simple shear, precluding the growth of the voids. The progress of the shear band plane, starting from the largest pore, is illustrated in cut-view pictures (e)-(f)-(g). Namely, large effective plastic strains emanating from the void are shown in cut-view picture (e). With the continuation of the loading process, the plastic strains front advances along the circumferential direction, see cut-view picture (g), ultimately leading to the formation of a plane with large plastic strains which represents the shear band. These results make apparent that the porous microstructure favors shear localization.

In fact, the comparison of the force evolution computed with the microstructure INC1Z-R3 and the fully dense material shows that the loss of load carrying capacity occurs much earlier for the porous material, see Fig. 3. The decrease in the specimen ductility caused by the porous microstructure is evaluated by computing the critical shear strain γ_c, defined as the shear strain corresponding to the angular displacement for which the force drops, ϕ_c. Namely, $\gamma_c^{\text{dense}} = \dfrac{d\,\phi_c^{\text{dense}}}{h} = 0.54$, and $\gamma_c^{\text{INC1Z-R3}} = 0.25$, i.e., the porous specimen displays roughly half ductility.

The porous microstructure also affects the location of the shear band. Fig. 4 shows the evolution of the effective plastic strain $\bar{\varepsilon}^p$ (measured along the path referred to as *lateral edge* in Fig. 1) versus the normalized axial coordinate $\bar{Z} = \frac{Z}{h}$ for the fully dense microstructure –Fig. 4a– and for the porous microstructure INC1Z-R3 –Fig. 4b–. The results correspond to different loading times in order to illustrate the inception of the shear band and the development of the localization process. The plot for the porous microstructure also includes the evolution of the local initial void volume fraction f_0^{local} calculated in slices whose length is one thousandth of the total length of the specimen.

Fig. 4a shows results for $t = 480$ μs, 520 μs, 535 μs and 550 μs. The greatest loading time corresponds to the loss of load carrying capacity of the sample. The progressive accumulation of strain at the central section of the specimen pictures the inception and development of the shear band. Notice that the shear band is located at

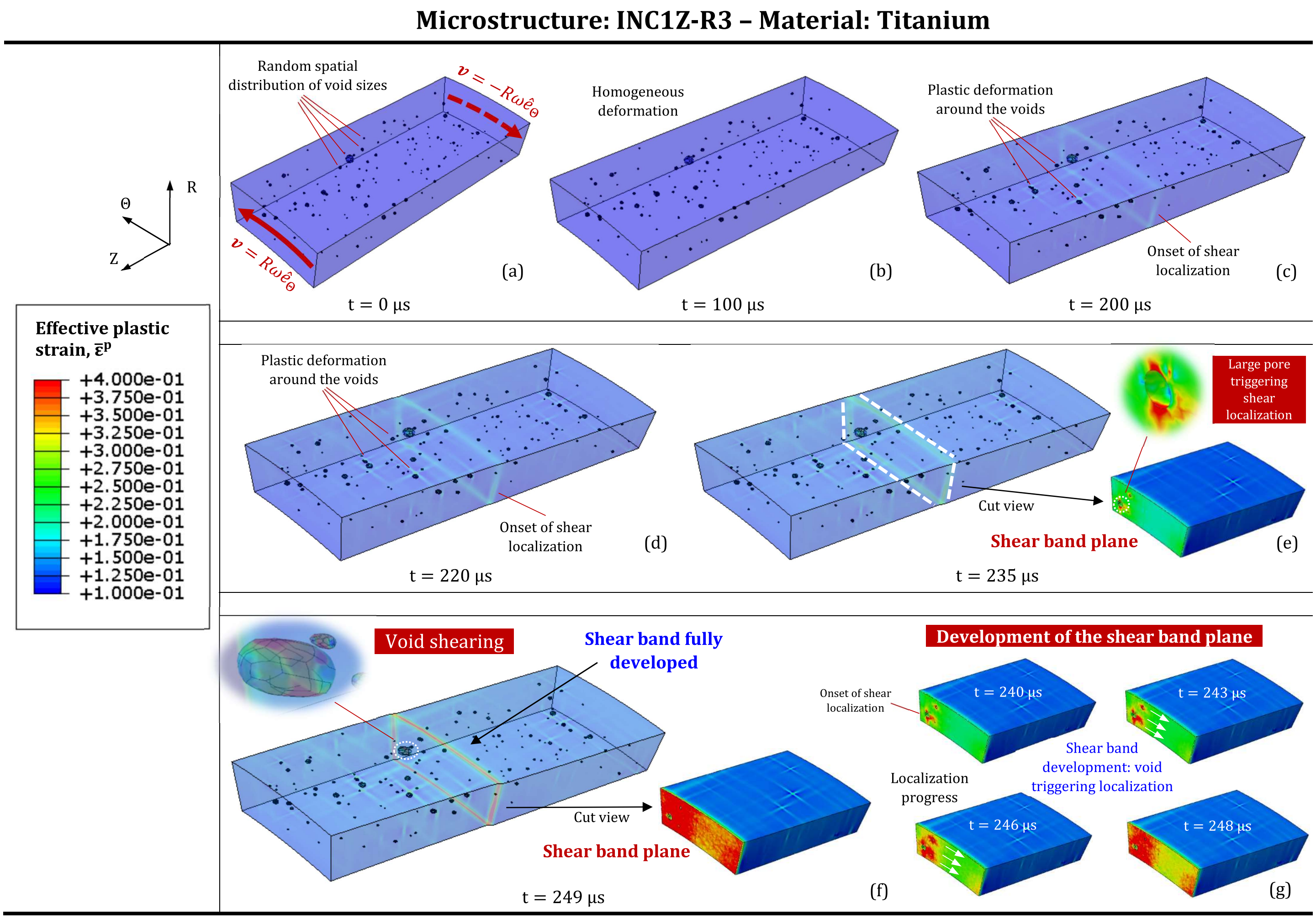

Figure 2: Microstructure INC1Z-R3. Material: Titanium. Nominal shear strain rate $\dot{\gamma}_0 = 1000$ s^{-1}. Contours of effective plastic strain $\bar{\varepsilon}$ for different loading times. Time evolution of the shear localization process: (a) $t = 0$ μs, (b) $t = 100$ μs, (c) $t = 200$ μs, (d) $t = 220$ μs, (e) $t = 235$ μs and (f) $t = 249$ μs. Development of the shear band plane for different loading times: (g) $t = 240$ μs, 243 μs, 246 μs and 248 μs.

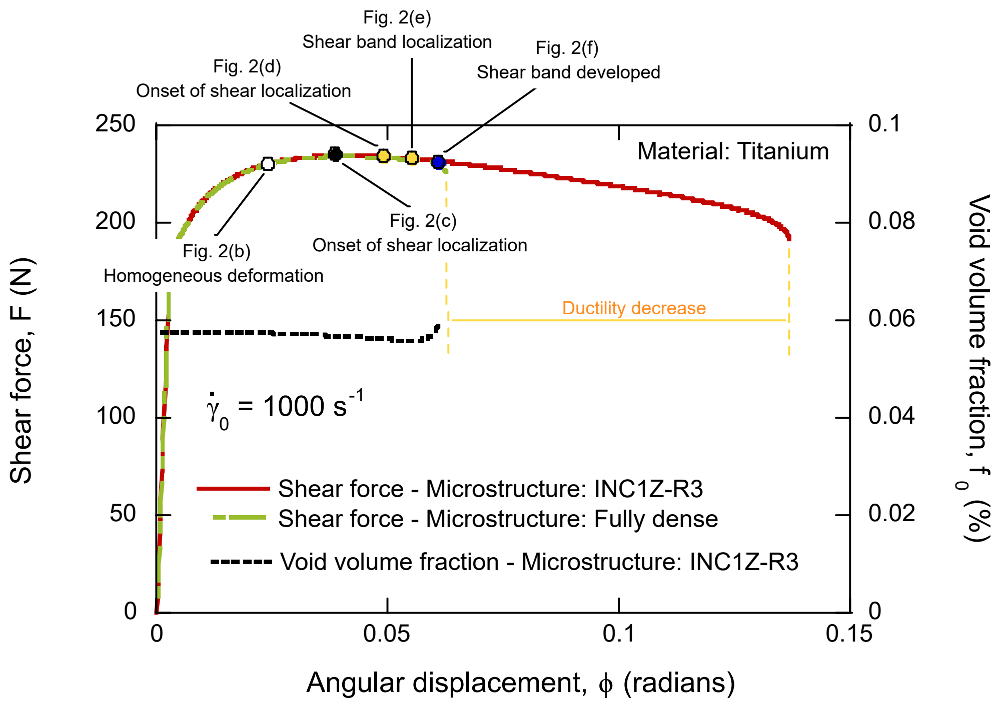

Figure 3: Shear force F and void volume fraction f_0 (%) versus angular displacement ϕ. Both the shear force and the angular displacement are measured at the *top surface* of the sample indicated in Fig. 1. Material: Titanium. Comparison between porous microstructure INC1Z-R3 and fully dense microstructure. Nominal shear strain rate $\dot{\gamma}_0 = 1000\ \mathrm{s}^{-1}$.

$Z = 0$ due to the symmetry of the problem for the fully dense microstructure.

Fig. 4b reports results for $t = 100\ \mu$s, 200 μs, 220 μs and 249 μs. These loading times correspond to pictures (b)-(c)-(d)-(f) in Fig. 2, so that for $t = 249\ \mu$s the specimen looses the load carrying capacity. Unlike for the fully dense material, for this porous microstructure the shear band is not located in the central section of the specimen, as the distribution of voids breaks the symmetry of the problem. The shear band is nucleated at the section of the sample with the largest local void volume fraction, which coincides with the largest pore of the distribution (as anticipated in Fig. 2).

4.2. The effect of microstructural realization

Fig. 5 shows the evolution of the shear force F versus the angular displacement ϕ for ten realizations of microstructure INC1Z (R1, R2, ... , R10) and two sets of material parameters corresponding to Titanium and HY-100 Steel, respectively (see Table 1). The $F - \phi$ curves for the different realizations overlap up to the angular displacement corresponding to the maximum force level is reached. With the continuation of the loading, the different realizations sequentially lose the load carrying capacity for angular displacements varying between 0.053 and 0.090 for Titanium, and between 0.083 and 0.147 for HY-100 Steel. Titanium is more prone to shear band formation for all realizations, most likely because of the higher value of the temperature sensitivity exponent.

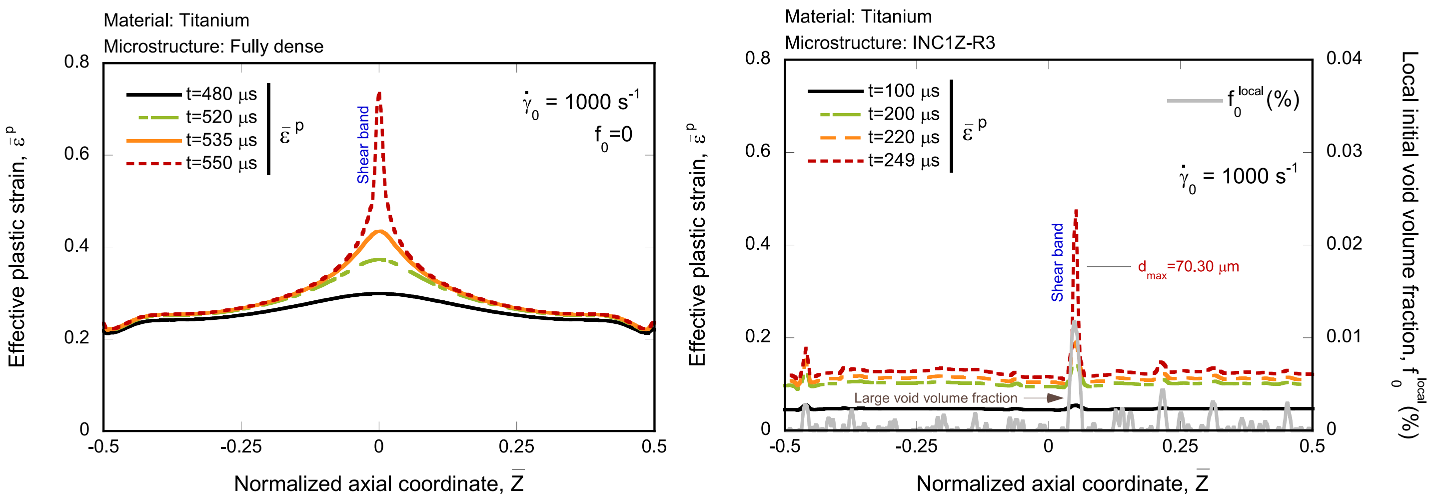

(a) (b)

Figure 4: Effective plastic strain $\bar{\varepsilon}^p$ versus normalized axial coordinate $\bar{Z} = \frac{Z}{h}$ for different loading times. The measurement path is referred to as *lateral edge* in Fig. 1. Material: Titanium. Nominal shear strain rate $\dot{\gamma}_0 = 1000$ s^{-1}. (a) Fully dense microstructure for $t = 480$ μs, 520 μs, 535 μs and 550 μs. (b) Porous microstructure INC1Z-R3 for $t = 100$ μs, 200 μs, 220 μs and 249 μs. The plot for the porous microstructure includes the evolution of the local initial void volume fraction $f_0^{local}(\%)$ along the normalized axial coordinate $\bar{Z}$.

Notice that the microstructural realization greatly affects the specimen ductility (recall that different realizations contain different spatial and void size distributions meeting the Log-normal statistical function fitted to the parent microstructure INC1Z, see Tables 2 and 3), which makes apparent the stochastic character of the shear band formation in porous materials submitted to dynamic twisting.

The effect of microstructural realization on the specimen ductility is further investigated in Fig. 6, which shows the evolution of the critical shear strain with the initial void volume fraction –Fig. 6a– and the maximum void diameter –Fig. 6b–. Each marker corresponds to a microstructural realization INC1Z (R1, R2, ... , R10). The numerical results have been fitted with solid red and dashed green power functions for Titanium and HY-100 Steel, respectively. Fig. 6a shows that the critical shear strain γ_c decreases nonlinearly with the initial void volume fraction f_0. The fitted curves for both Titanium and HY-100 Steel display a concave-upward shape. Note that the scatter in the finite element results is greater for low values of the initial void volume fraction, such that the fitting with the power functions improves as f_0 increases. Based on the fitted curves, the relative drop in ductility for the range of initial void volume fractions considered is $\left.\dfrac{\gamma^c|_{f_0=0.039\,\%} - \gamma^c|_{f_0=0.132\,\%}}{\gamma^c|_{f_0=0.132\,\%}}\right|_{\text{Titanium}} = 48\ \%$ and $\left.\dfrac{\gamma^c|_{f_0=0.039\,\%} - \gamma^c|_{f_0=0.132\,\%}}{\gamma^c|_{f_0=0.132\,\%}}\right|_{\text{HY}-100\text{ Steel}} = 53\ \%$, respectively, for the two sets of material parameters investigated.

Fig. 6b shows that the critical shear strain also decreases nonlinearly with the maximum void diameter. The key difference with the results shown in Fig. 6a is that the numerical calculations all lie very close to the fitted

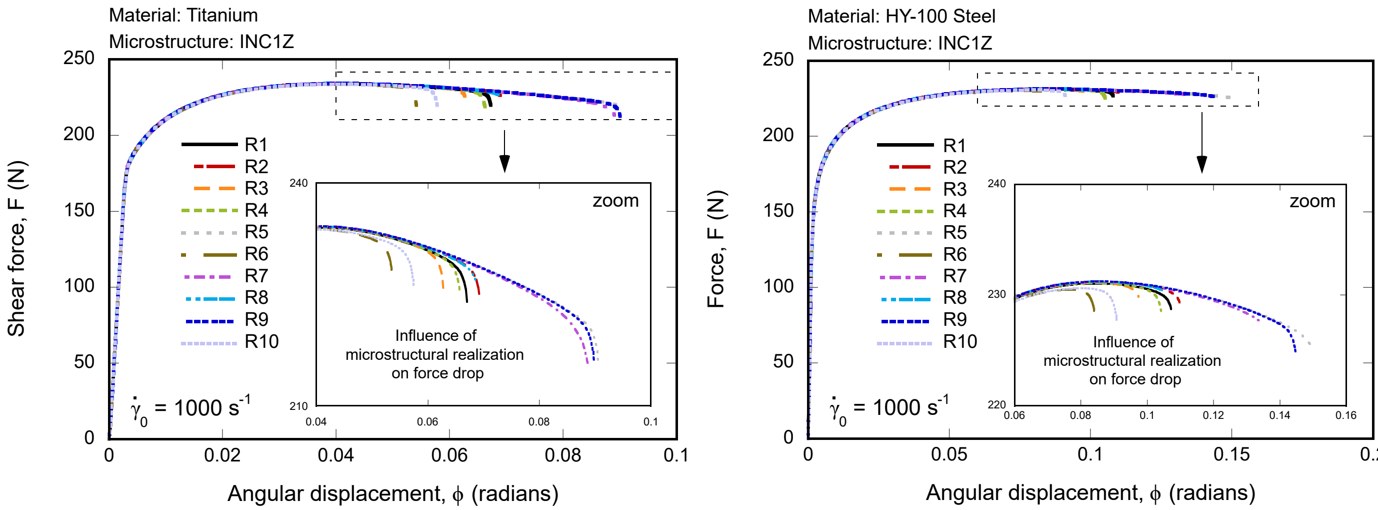

(a) (b)

Figure 5: Shear force F versus angular displacement ϕ measured at the *top surface* of the sample indicated in Fig. 1. Nominal shear strain rate $\dot{\gamma}_0 = 1000$ s^{-1}. Comparison between ten realizations of microstructure INC1Z (R1, R2, ... , R10). Material: (a) Titanium and (b) HY-100 Steel.

power function, and show very small scatter within the range of values of d_{max} investigated. This suggests that the maximum void diameter is the feature of the porous microstructure with greatest impact on the specimen ductility (we will further elaborate on this issue in Section 4.3). Attending to the fitted curves, the relative drop of the critical shear strain for the range of maximum void diameters considered is $\left.\dfrac{\gamma^c|_{d_{max}=38.83\,\mu\text{m}} - \gamma^c|_{d_{max}=86.77\,\mu\text{m}}}{\gamma^c|_{d_{max}=86.77\,\mu\text{m}}}\right|_{\text{Titanium}} = 69\ \%$ and $\left.\dfrac{\gamma^c|_{d_{max}=38.83\,\mu\text{m}} - \gamma^c|_{d_{max}=86.77\,\mu\text{m}}}{\gamma^c|_{d_{max}=86.77\,\mu\text{m}}}\right|_{\text{HY}-100\text{ Steel}} = 81\ \%$, for Titanium and HY-100 Steel, respectively.

The location of the shear band in the specimen also depends on the microstructural realization. Fig. 7 shows contours of effective plastic strain for R1, R2, R5, R6, R7 and R10, for the loading time at which the specimen looses the load carrying capacity. The color coding is the same used in Fig. 2 and the material parameters correspond to Titanium. For the same realizations, Fig. 8 displays the evolution of the effective plastic strain and the local initial void volume fraction along the normalized axial coordinate, indicating the location and size of the three larger pores of the microstructure. The results for R1 in Figs. 7a and 8a show the main shear band developing at $\bar{Z} \approx -0.27$, and secondary localization zones located at $\bar{Z} \approx 0.21$ and 0.39. Both primary and secondary localizations occur at sections of the sample with high initial void volume fraction due to the presence of large pores. For realization R2 –see Figs. 7b and 8b– the main shear band located at $\bar{Z} = -0.19$ stands out with respect to other excursions of strain which correspond to secondary localization zones. The main shear band is triggered by the largest pore of the microstructure. The results in Figs. 7c and 8c correspond to R5, which displays the smaller value of d_{max} of all realizations, see Table 3. The principal shear band is located at $\bar{Z} = 0.25$, which

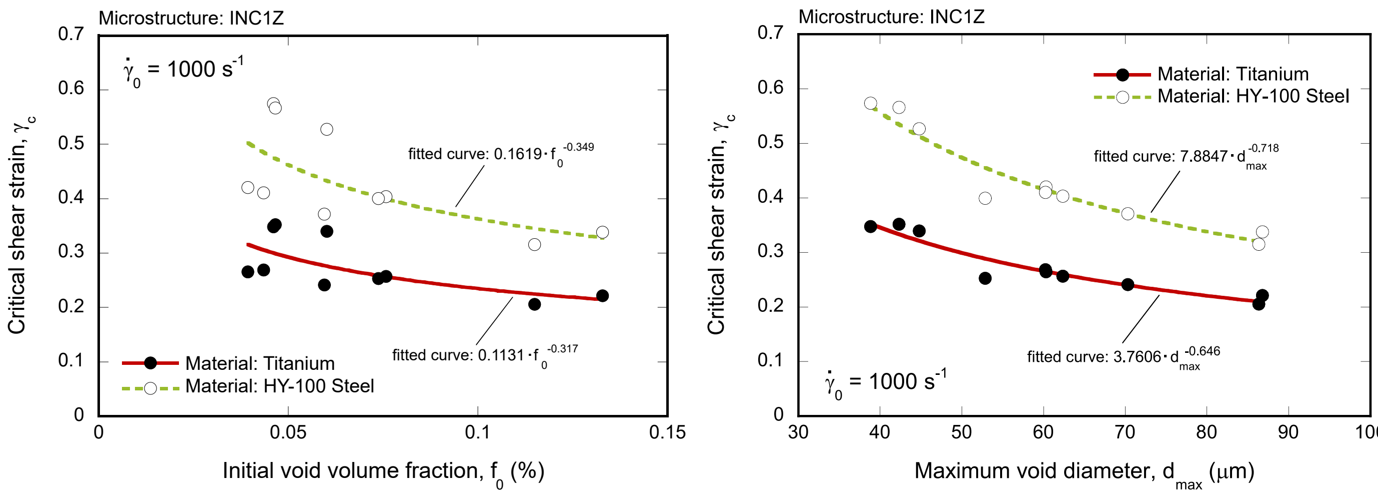

(a) (b)

Figure 6: Results corresponding to ten realizations of microstructure INC1Z (R1, R2, ... , R10) for Titanium and HY-100 Steel. Nominal shear strain rate $\dot{\gamma}_0 = 1000$ s^{-1}. Evolution of the critical shear strain leading to shear band formation γ_c with (a) the initial void volume fraction $f_0(\%)$ and (b) the maximum void diameter d_{max}.

corresponds to the location of the largest void, but there are multiple excursions of strain representing secondary localization bands. Note that the difference in the peak strain between the main shear band and the secondary localizations is comparatively less than for realization R2. This is most likely because the maximum void size is smaller, which delays the loss of load carrying capacity of the specimen (360 μs is the greatest loading time of all realizations) and favors plastic localization around pores other than the greatest void of the microstructure (the difference in size between the greatest void and these other pores which trigger secondary localizations is small). For realization R6, the results in Figs. 7d and 8d show a large excursion of strain at the section of the sample where the void volume fraction is higher, where a large pore of diameter 86.33 μm is located. Together with R10, realization R6 contains the largest void of all realizations, see Table 3, and displays the shortest loading time for which the specimen losses of load carrying capacity ($t = 217$ μs). On the other hand, realization R7 displays the second smallest value of d_{max}, and similarly to R5, there are several secondary localization bands in the specimen, see Figs. 7e and 8e. It is apparent that if the largest void of the microstructure does not stand out with respect to other pores, the specimen is prone to develop several secondary localization bands, and the main shear band may be triggered by other pore than the largest. Notice also that R7 shows the second largest loading time for which the specimen loses the capacity of carrying load ($t = 353$ μs), just behind R5. Moreover, Figs. 7f and 8f show the results for realization R10, which contains the largest void together with realization R6 (as mentioned before). The main shear band is located at $\bar{Z} = 0.31$, at the location of the largest void, and there is a secondary localization at $\bar{Z} = -0.43$ triggered by a void of 70.46 μm diameter (second largest void of R10 for which $d_{max} = 86.77$ μm).

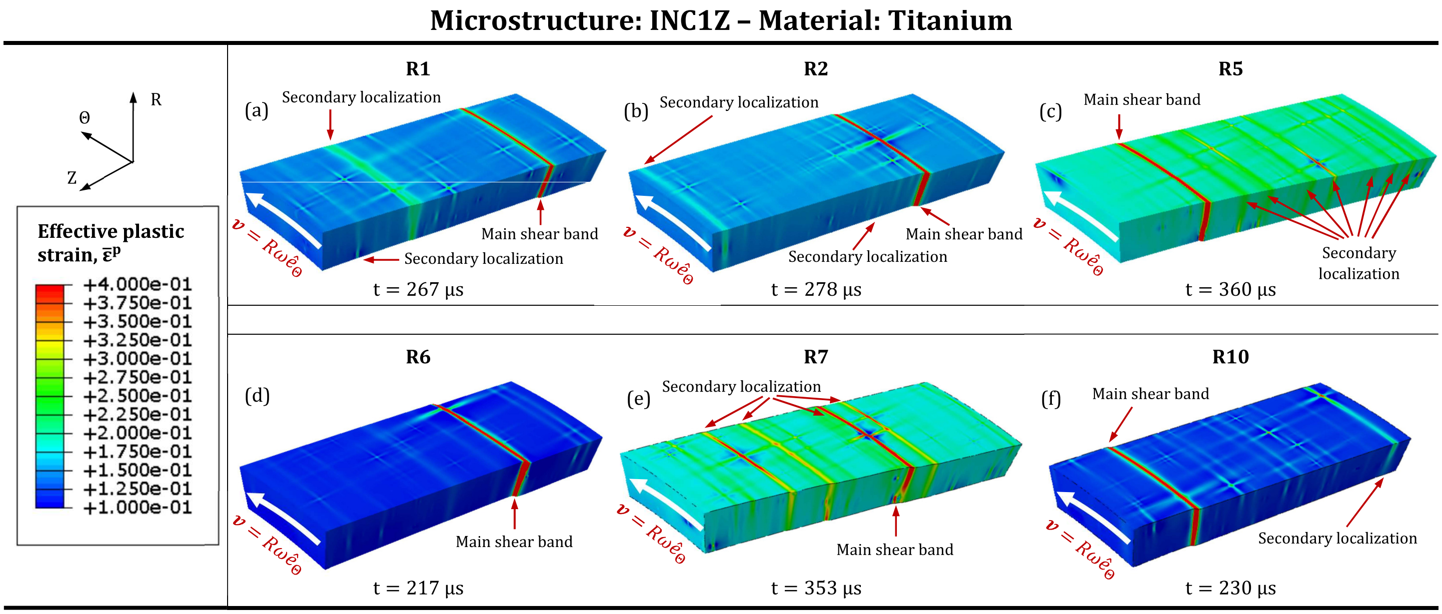

Figure 7: Microstructure: INC1Z. Material: Titanium. Nominal shear strain rate $\dot{\gamma}_0 = 1000\ \mathrm{s}^{-1}$. Contours of effective plastic strain $\bar{\varepsilon}^p$ for different microstructural realizations: (a) R1, (b) R2, (c) R5, (d) R6, (e) R7 and (f) R10.

We have performed the same analysis with HY-100 Steel to substantiate the outcomes of the calculations with different material behaviors. For the sake of brevity, Fig. 9 only shows realizations R2 and R6. The results are qualitatively the same obtained with Titanium (compare Figs. 8b-d with Figs. 9a-b), so that the main shear band is located at the same axial coordinate. The quantitative difference is that localization occurs later in time for the HY-100 Steel specimens (as already shown in Figs. 5 and 6), so that the ratio between the peak strain in the main shear band and the strain outside the main shear band when the sample loses the load carrying capacity is greater for Titanium. These results make apparent that, irrespective of the material parameters, the position of the shear band is generally dictated by the location of the largest pore of the microstructure.

4.3. The effect of microstructure

Fig. 10 shows the evolution of the shear force with the angular displacement for calculations performed with three realizations (R1, R2, R3) of microstructures Al3XY, SS5XY and Ti0.5XY (recall that results for these microstructures were not shown in Sections 4.1 and 4.2). All the results reported in this section are obtained with the material parameters corresponding to Titanium. The calculations with SS5XY and Ti0.5XY show similar $F-\phi$ curves, with the value of the angular displacement for which the force drops varying with the microstructural realization. Note that both the initial void volume fraction and the maximum void diameter are relatively similar for SS5XY and Ti0.5XY, see Tabel 3. In contrast, for Al3XY the maximum force is lower and the loss of load

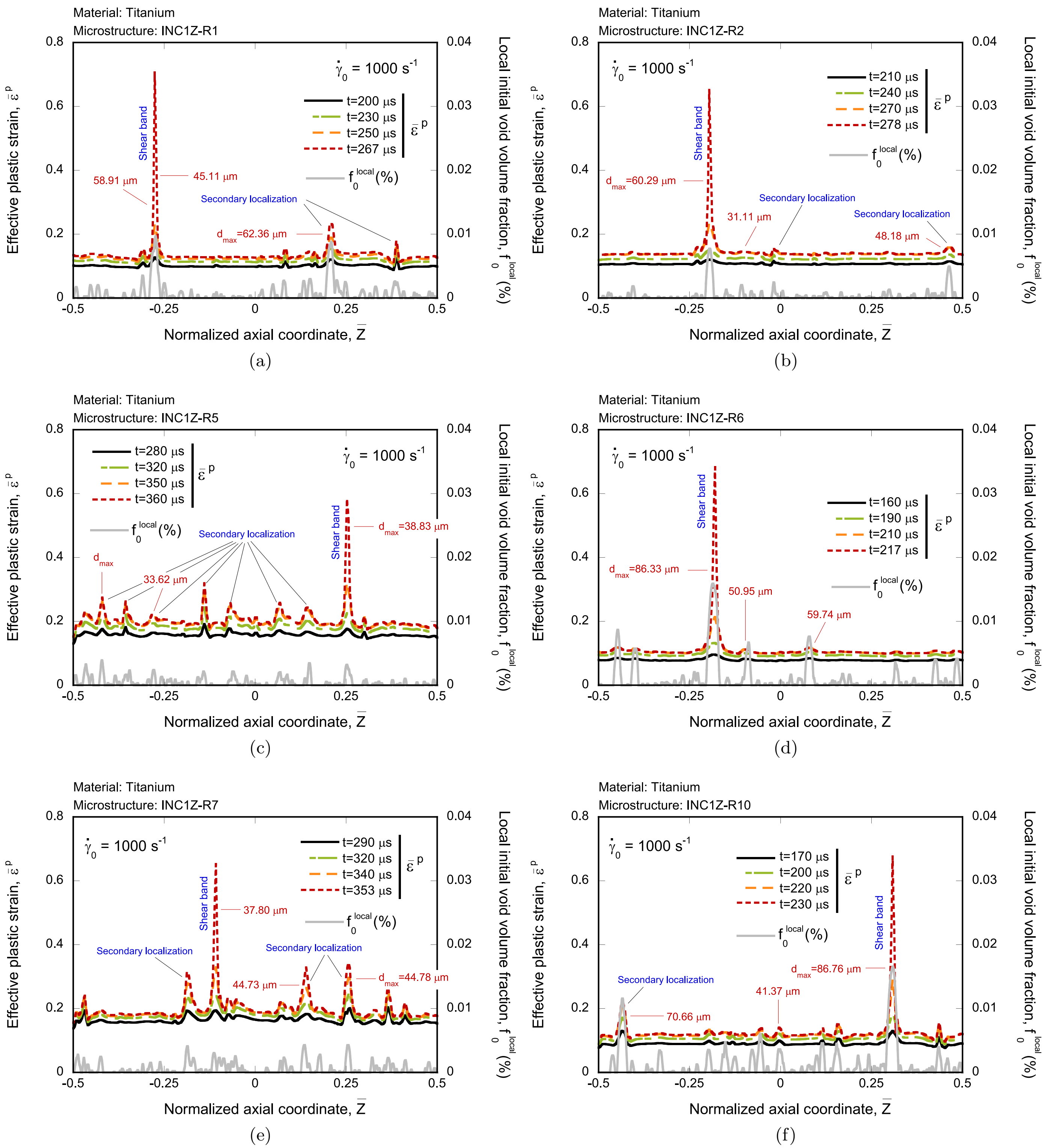

Figure 8: Effective plastic strain $\bar{\varepsilon}^p$ and local initial void volume fraction $f_0^{local}(\%)$ versus normalized axial coordinate $\bar{Z} = \frac{Z}{h}$. The measurement path is referred to as *lateral edge* in Fig. 1. The results for the effective plastic strain correspond to different loading times. Material: Titanium. Nominal shear strain rate $\dot{\gamma}_0 = 1000$ s^{-1}. Results corresponding to different microstructural realizations: (a) R1, (b) R2, (c) R5, (d) R6, (e) R7 and (f) R10.

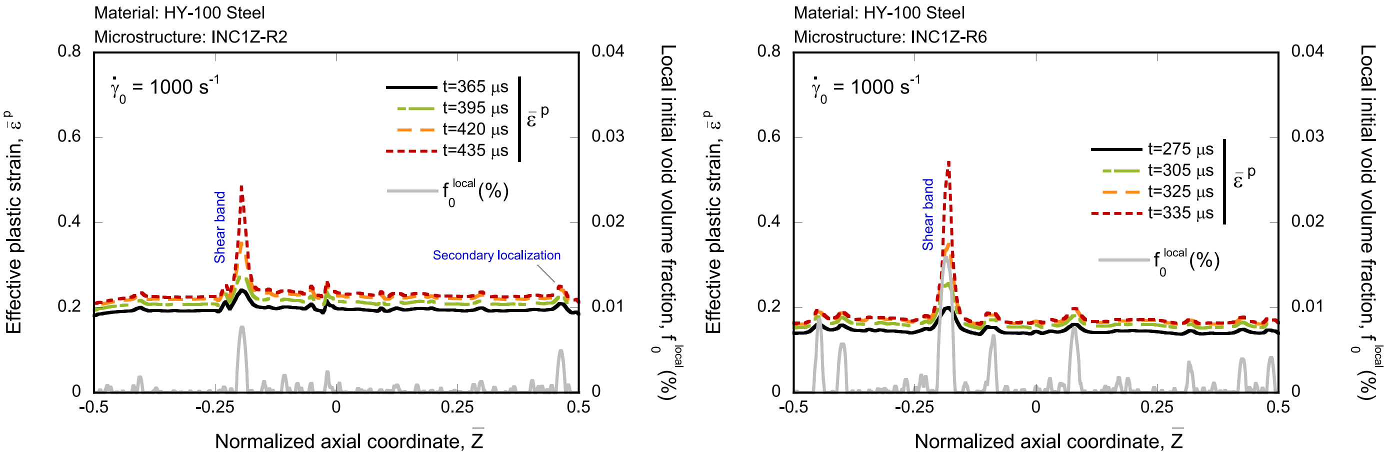

(a) (b)

Figure 9: Effective plastic strain $\bar{\varepsilon}^p$ and local initial void volume fraction $f_0^{local}(\%)$ versus normalized axial coordinate $\bar{Z} = \frac{Z}{h}$. The measurement path is referred to as *lateral edge* in Fig. 1. The results for the effective plastic strain correspond to different loading times. Material: HY-100 Steel. Nominal shear strain rate $\dot{\gamma}_0 = 1000$ s^{-1}. Results corresponding to different microstructural realizations: (a) R2 and (b) R6.

carrying capacity occurs rather earlier due to the larger porosity and the greater voids of this microstructure, see Tabel 3 (≈ 1.5 % of initial void volume fraction lowers ≈ 3 % the maximum force).

The influence of porous microstructure on the specimen ductility is further investigated in Fig. 11, which shows the evolution of the critical shear strain leading to shear band formation γ_c with the initial void volume fraction f_0 –Fig. 11a– and the maximum void diameter d_{max} –Fig. 11b–. The results for microstructures Al3XY, SS5XY and Ti0.5XY correspond to the black markers, the green markers are the calculations for the ten realizations with microstructure INC1Z, and the solid red lines are the power functions fitted to the green markers in Fig. 6.

Consistent with the results obtained for INC1Z, the calculations with microstructures Al3XY, SS5XY and Ti0.5XY show that the critical shear strain decreases nonlinearly with both f_0 and d_{max}. However, the computations for large values of f_0, which correspond to Al3XY, lie above the fitted curve, see Fig. 11a, suggesting that increasing the void volume fraction alone does not lead to an important drop in the sample ductility (we have also included in Fig. 11a the critical shear strains computed from the calculations reported in Section 5 which also lie above the fitted curve). In contrast, all the results with microstructures Al3XY, SS5XY and Ti0.5XY lie very close to the fitted curve for the evolution of the critical shear strain with the maximum void diameter, see Fig. 11b, reinforcing the idea that d_{max} is the main microstructural parameter controlling the specimen ductility (we have also included in Fig. 11b the critical shear strains computed from the calculations reported in Section 5 which also lie very close to the fitted curve). These results find resemblance with the analytical calculations reported in Fig.

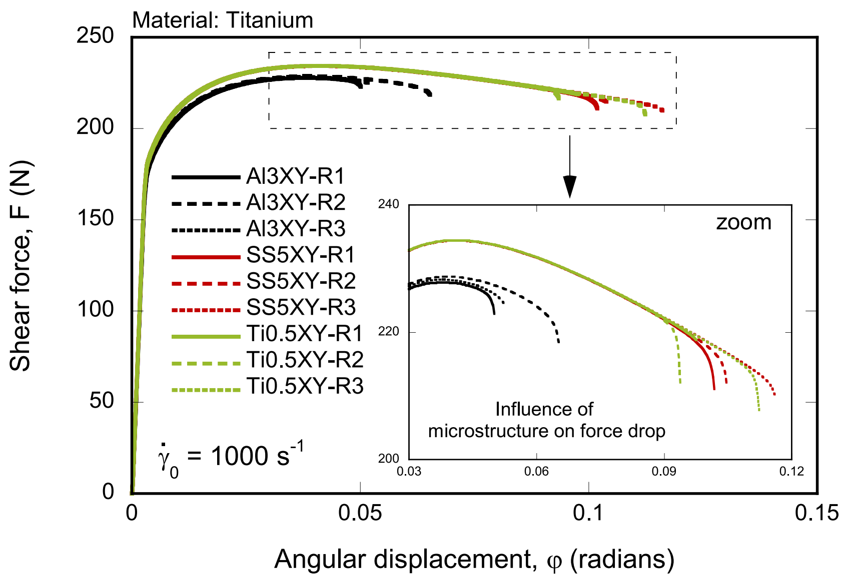

Figure 10: Shear force F versus angular displacement ϕ measured at the *top surface* of the sample indicated in Fig. 1. Material: Titanium. Results corresponding to microstructures Al3XY, SS5XY and Ti0.5XY for realizations R1, R2 and R3. Nominal shear strain rate $\dot{\gamma}_0 = 1000 \text{ s}^{-1}$.

2 of Molinari and Clifton (1987) showing that the critical shear strain decreases nonlinearly with the amplitude of geometrical perturbations (geometric defects, instead of the material defects represented by the voids in the calculations of this paper).

Fig. 12 displays contours of effective plastic strain for the calculations performed with microstructures Al3XY, SS5XY and Ti0.5XY (3 realizations per microstructure), for the loading time corresponding to the loss of load carrying capacity of the samples. The color coding is the same used in Figs. 2 and 7. The semi-transparent view shows the porous microstructure of the specimens. For the same calculations, Fig. 13 pictures the evolution of the effective plastic strain in the specimen and the local initial void volume fraction along the normalized axial coordinate.

The isocontours for microstructure Al3XY –Figs. 12abc– show many more pores than for any other microstructure, and many secondary localization zones in addition to the main shear band. The large number of pores makes the largest void do not stand out with respect to other voids in the microstructure (e.g., the diameter of the three largest pores for Al3XY-R2 is very similar, 69.00 μm, 66.98 μm and 64.47 μm, respectively, with less than 7 % difference between the first and the third larger pore), and there are no sections of the sample that comparatively have much larger value of the initial void volume fraction –Figs 13abc–, so that the $\bar{\varepsilon}^p - \bar{Z}$ curves display a continuous succession of peaks and valleys (many pores trigger shear localization). In contrast, for microstructures SS5XY and Ti0.5XY, the number of voids is much lower, and so is the number of secondary localizations (the diameter of the

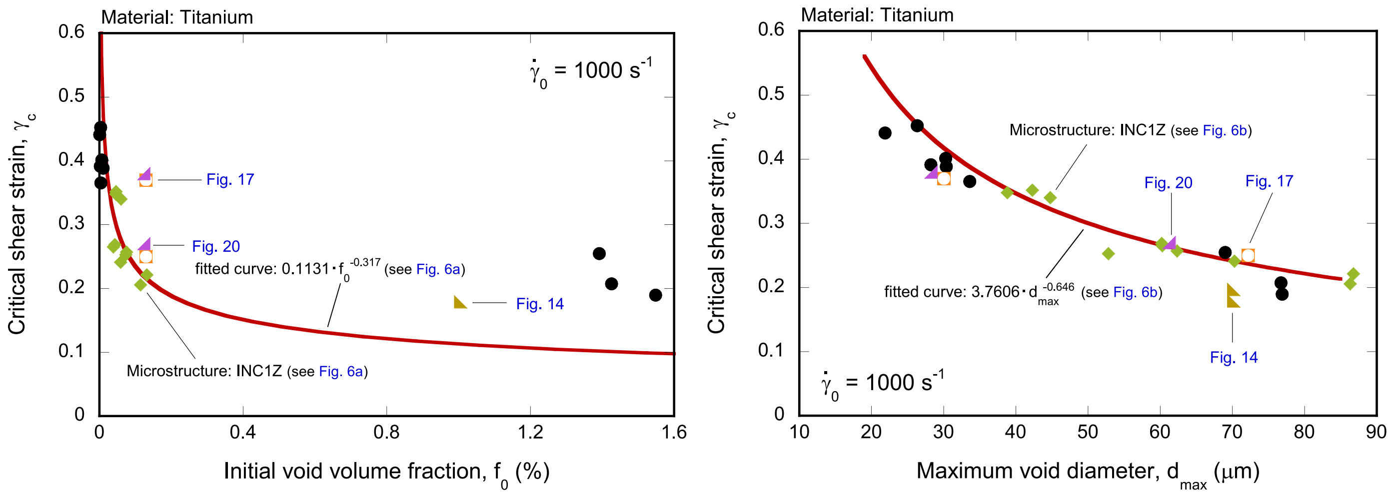

(a) (b)

Figure 11: Results corresponding to microstructures Al3XY, SS5XY and Ti0.5XY for realizations R1, R2 and R3. Comparison with the ten realizations of microstructure INC1Z (R1, R2, ... , R10) shown in Fig. 6. Nominal shear strain rate $\dot{\gamma}_0 = 1000$ s^{-1}. Evolution of the critical shear strain leading to shear band formation γ_c with (a) the initial void volume fraction f_0 (%) and (b) the maximum void diameter d_{max}. We have also included the critical shear strains computed from the calculations reported in Section 5.

three largest voids for SS5XY-R2 and Ti0.5XY-R2 is 30.27 μm, 27.76 μm and 25.05 μm, and 33.60 μm, 30.32 μm and 14.57 μm, respectively). For instance, the realizations with Ti0.5XY only contain between 3 and 6 voids, and the void volume fraction varies from 0.001 % to 0.004 %, see Table 3, such that there is only one or no secondary localizations, see Fig. 13ghi, and the main shear band is nucleated at the section –or very close to the section– of the sample where the largest pore is located, which stands out with respect to other voids of the microstructure (more than 45 %, 48 % and 55 % difference between the first and the third larger pore for realizations R1, R2 and R3, respectively). Likewise, the realizations for SS5XY in Figs. 12def show several secondary localizations (but many less than for Al3XY), as they contain more pores than the calculations with Ti0.5XY, see also Table 3. The main shear band and the secondary localizations are generally nucleated at the sections where the largest pores of the microstructure are located, see Figs. 13def. The exception is SSXY-R3, Fig. 13f, because the largest void is very close to the end of the sample $\bar{Z} = -0.49$, and the application of the velocity boundary condition prevents localization at this location. In the case of SSXY-R3 the main shear band is triggered by the fourth largest pore of the microstructure with diameter 18.80 μm and located at $\bar{Z} = -0.007$.

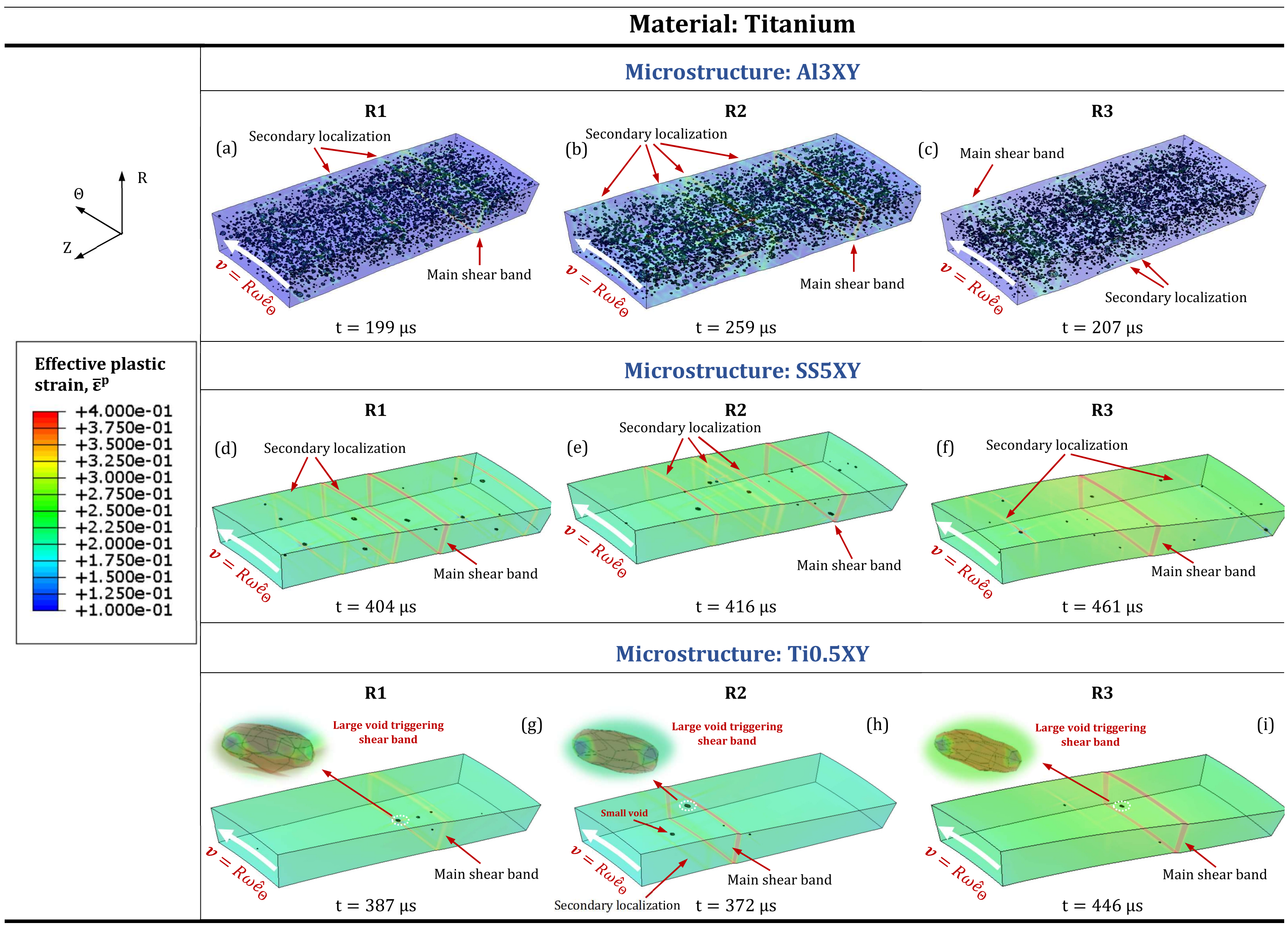

Figure 12: Material: Titanium. Nominal shear strain rate $\dot{\gamma}_0 = 1000\ \mathrm{s}^{-1}$. Contours of effective plastic strain $\bar{\varepsilon}$ for different microstructures: (a)-(b)-(c) Al3XY for R1, R2 and R3, (d)-(e)-(f) SS5XY for R1, R2 and R3 and (g)-(h)-(i) Ti0.5XY for R1, R2 and R3.

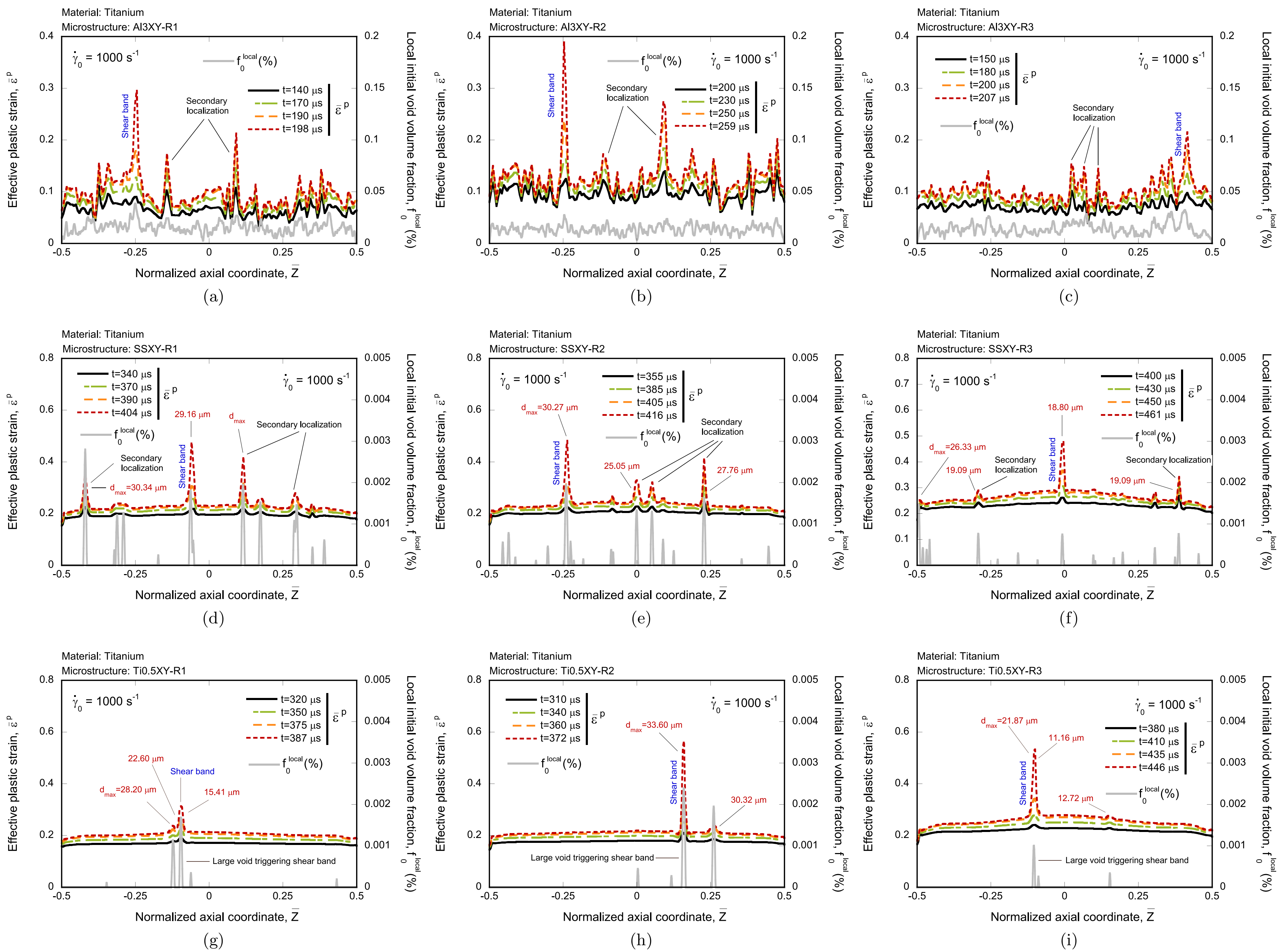

Figure 13: Effective plastic strain $\bar{\varepsilon}^p$ and local initial void volume fraction $f_0^{local}(\%)$ versus normalized axial coordinate $\bar{Z} = \frac{Z}{h}$. The measurement path is referred to as *lateral edge* in Fig. 1. The results for the effective plastic strain correspond to different loading times. Material: Titanium. Nominal shear strain rate $\dot{\gamma}_0 = 1000\ \text{s}^{-1}$. Results corresponding to different microstructures: (a)-(b)-(c) Al3XY for R1, R2 and R3, (d)-(e)-(f) SS5XY for R1, R2 and R3 and (g)-(h)-(i) Ti0.5XY for R1, R2 and R3.

5. Parametric analysis: porosity effects

The finite element simulations reported in this section correspond to *virtual* porous microstructures created from INC1Z-R1 (hereinafter referred to as parent microstructural realization). All calculations have been carried out for $\dot{\gamma}_0 = 1000 \text{ s}^{-1}$ with material parameters corresponding to Titanium. In Section 5.1, we compare calculations with different void volume fractions obtained by varying the number of pores in the microstructure, while keeping the distribution of void sizes and the maximum pore size the same. Moreover, Section 5.2 shows calculations with the same void volume fraction but different void size distributions obtained by varying the mean and the standard deviation of the Log-normal statistical function fitted to the parent microstructure (see Table 2).

5.1. The effect of void volume fraction

The calculations have been performed for two different initial void volume fractions, $f_0 = 1$ % and 2 %. The maximum void diameter is $d_{max} = 69.90$ μm, while the mean and the standard devitation of the distribution of void sizes are $\mu = 16.58$ μm and $dev = 7.71$ μm, respectively (the same of INC1Z, see Table 2). The number of voids in the specimens with $f_0 = 1$ % and 2 % is 2031 and 4119, respectively. For $f_0 = 1$ % there are two voids with diameter 69.90 μm, and the third largest pore of the microstructure has a diameter of 62.60 μm, while for $f_0 = 2$ % the size of the seven largest pores is 69.90 μm. The large number of pores prevents that any void stands out with respect to other voids in the microstructure (similar to the case of microstructure Al3XY, see Section 4.3).

Fig. 14 shows the evolution of the shear force and the void volume fraction with the angular displacement ϕ for both initial void volume fractions considered. The calculation for $f_0 = 2$ % displays lower peak force, and the loss of load carrying capacity occurs earlier. The critical shear strains for $f_0 = 1$ % and 2 % are 0.197 and 0.179, respectively, so that doubling the value of f_0 leads to a (mild) decrease in the specimen ductility of 9 % (the reader is referred to Fig. 11a to check that these results are above the fitted curve). The void volume fraction in the specimen, for both values of f_0, is virtually constant during loading (see also Fig. 3).

Fig. 15 shows the evolution of the effective plastic strain $\bar{\varepsilon}^p$ and the local initial void volume fraction f_0^{local} versus the normalized axial coordinate $\bar{Z}$. The $\bar{\varepsilon}^p - \bar{Z}$ curves show a continuous succession of peaks an valleys, as many pores trigger localization (see also Fig. 13abc). For $f_0 = 1$ %, see Fig. 15a, the main shear band and the two most developed secondary localizations are located at the sections of the sample with larger value of the local void volume fraction, which correspond to the locations of the three larger pores of the microstructure $\bar{Z} = 0.18$,

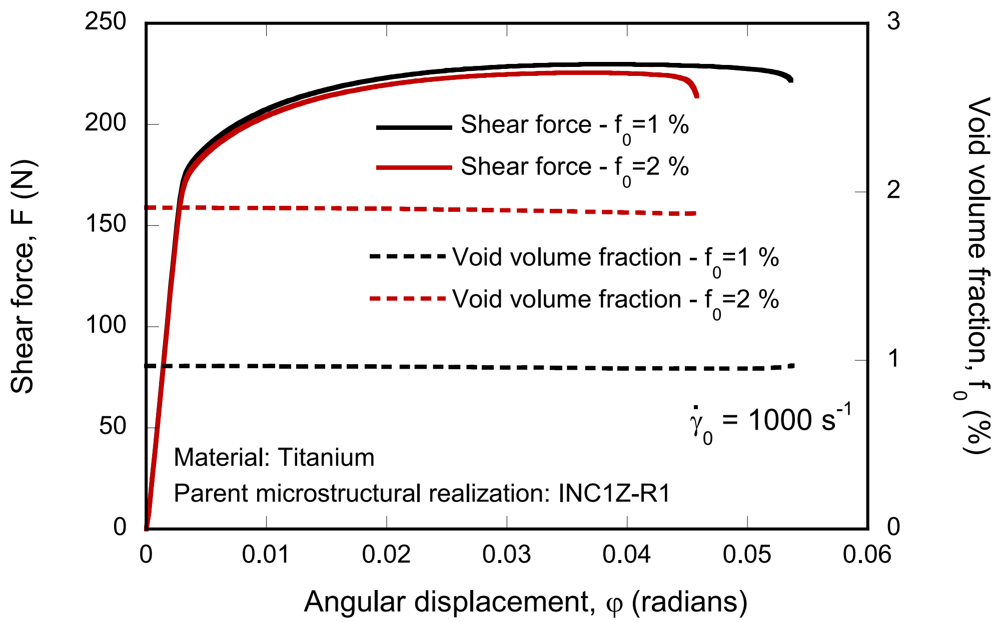

Figure 14: Shear force F and void volume fraction f_0 (%) versus angular displacement ϕ. Both the shear force and the angular displacement are measured at the *top surface* of the sample indicated in Fig. 1. Material: Titanium. Parent microstructural realization: INC1Z-R1. Nominal shear strain rate $\dot{\gamma}_0 = 1000$ s^{-1}. Results corresponding to two different initial void volume fractions: $f_0 = 1$ % and $f_0 = 2$ %.

-0.06 and -0.18. These three excursions of strain are highlighted in the contour plot of Fig. 16a. For $f_0 = 2$ %, see Fig. 15b, while there are no sections of the sample with comparatively much higher value of the initial void volume fraction, the main shear band indicated in Fig. 16b is also triggered by one of the largest pores of the microstructure which is located at $\bar{Z} = 0.20$. These results make apparent the role of large pores on shear band formation. In the case that there are many large pores of the same size in the microstructure, any of these large pores can give rise to the main shear band, depending on its relative position with respect to other pores and the formation of clusters which may favor localization.

5.2. The effect of voids size

The calculations have been performed for different void size distributions while keeping constant the initial void volume fraction $f_0 = 0.13$ %. Namely, we have generated two distributions with mean voids size of $\mu = 10$ μm and 30 μm in which the standard deviation is 45 % of the mean value, and two distributions in which the standard deviation is 18 % and 60 %, respectively, with the average pore diameter being $\mu = 16.58$ μm (the same of the parent microstructure, see Table 2).

Fig. 17 shows the shear force F versus the angular displacement ϕ for the distributions with mean $\mu = 10$ μm and 30 μm. These two microstructures contain 1456 and 50 pores, respectively (see the semi-transparent view of

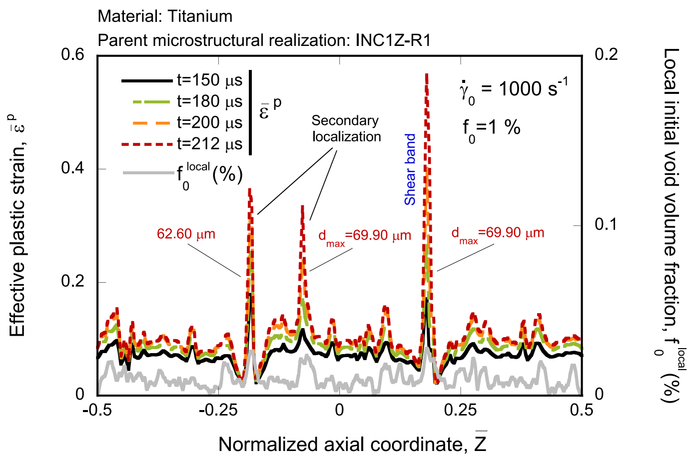

(a)

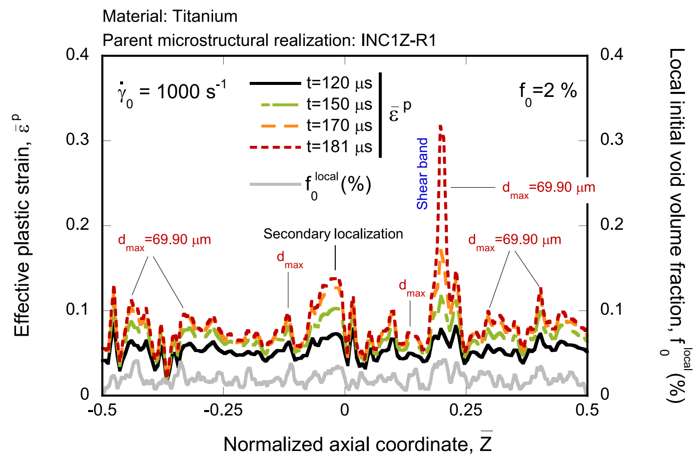

(b)

Figure 15: Effective plastic strain $\bar{\varepsilon}^p$ and local initial void volume fraction $f_0^{local}(\%)$ versus normalized axial coordinate $\bar{Z} = \frac{Z}{h}$. The measurement path is referred to as *lateral edge* in Fig. 1. The results for the effective plastic strain correspond to different loading times. Material: Titanium. Parent microstructural realization: INC1Z-R1. Nominal shear strain rate $\dot{\gamma}_0 = 1000$ s^{-1}. Results corresponding to two values of the initial void volume fraction: (a) $f_0 = 1$ % and (b) $f_0 = 2$ %.

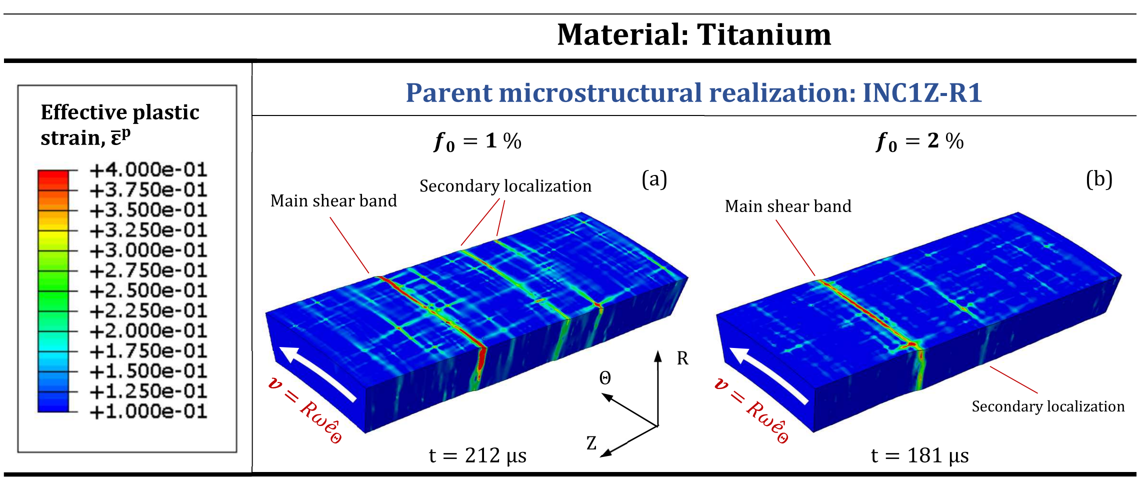

Figure 16: Parent microstructural realization: INC1Z-R1. Material: Titanium. Nominal shear strain rate $\dot{\gamma}_0 = 1000$ s^{-1}. Contours of effective plastic strain $\bar{\varepsilon}$ for two values of the initial void volume fraction: (a) $f_0 = 1$ % and (b) $f_0 = 2$ %.

the specimens in Fig. 19). The diameter of the three largest pores for $\mu = 30$ μm is 72.19 μm, 64.12 μm and 58.94 μm, while in the case of $\mu = 10$ μm the three largest pores have the same size 30.03 μm. The loss of load carrying capacity occurs earlier for the microstructure with larger mean void size, since greater pores favor shear band formation. Namely, the critical shear strains for $\mu = 10$ μm and $\mu = 30$ μm are 0.37 and 0.25, so that tripling the average pore size, while increasing the maximum void size by ≈ 42 μm, leads to a decrease of 32 % in the specimen ductility (the reader is referred to Fig. 11b to check the correlation of these results with the fitted curve).

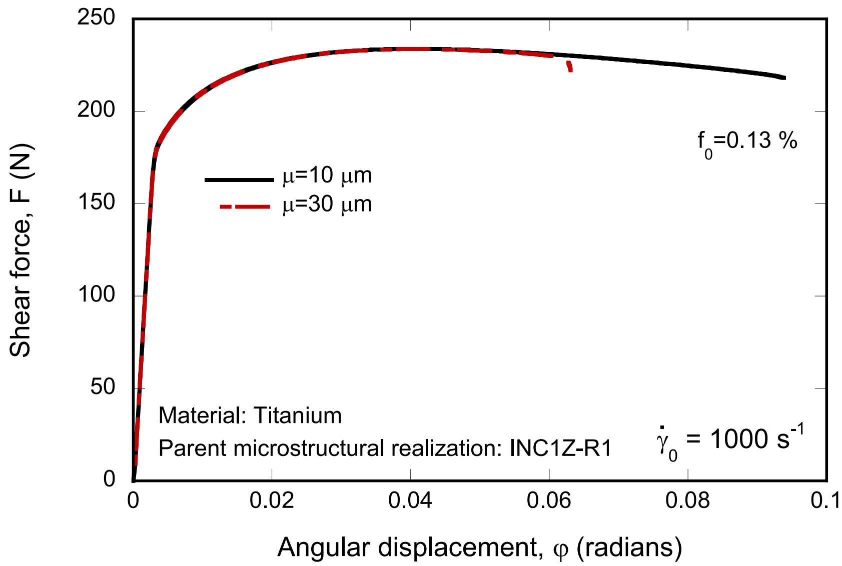

Figure 17: Shear force F versus angular displacement ϕ measured at the *top surface* of the specimen indicated in Fig. 1. Material: Titanium. Parent microstructural realization: INC1Z-R1. Nominal shear strain rate $\dot{\gamma}_0 = 1000$ s^{-1}. Initial void volume fraction $f_0 = 0.13$ %. Results corresponding to two different values of the mean voids size: $\mu = 10$ μm and $\mu = 30$ μm.

Fig. 18 displays the evolution of the effective plastic strain $\bar{\varepsilon}^p$ and the local initial void volume fraction f_0^{local} versus the normalized axial coordinate $\bar{Z}$. The results for $\mu = 10$ μm in Fig. 18a show a series of peaks and valleys, similar to Figs. 13abc, as the microstructure contains a large number of pores, which promotes the nucleation of many localization bands, see the isocontours of Fig. 19a. Still, the main excursions of strain are located at the sections of the sample which contain some of the larger voids of the microstructure. The results for $\mu = 30$ μm in Fig. 18b show a large excursion of strain corresponding to the main shear band, which is triggered at the location of the largest pore of the microstructure, see Fig. 19b. The two secondary localizations triggered by the second and third larger voids are comparatively much less developed. These results suggest that decreasing the number of pores while increasing their size makes the largest voids of the microstructure to have an increasing effect on the localization pattern, which is formed by less localization bands, with the main shear band standing out over the secondary localizations.

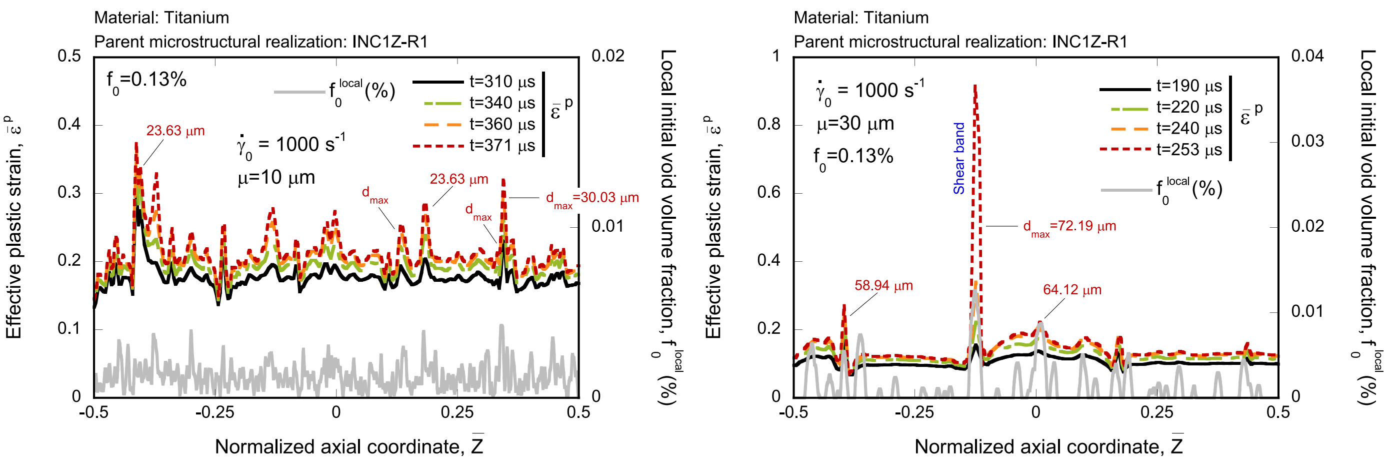

(a) (b)

Figure 18: Effective plastic strain $\bar{\varepsilon}^p$ and local initial void volume fraction $f_0^{local}(\%)$ versus normalized axial coordinate $\bar{Z} = \frac{Z}{h}$. The measurement path is referred to as *lateral edge* in Fig. 1. The results for the effective plastic strain correspond to different loading times. Material: Titanium. Parent microstructural realization: INC1Z-R1. Nominal shear strain rate $\dot{\gamma}_0 = 1000$ s^{-1}. Initial void volume fraction $f_0 = 0.13$ %. Results corresponding to two different values of the mean voids size: (a) $\mu = 10$ μm and (b) $\mu = 30$ μm.

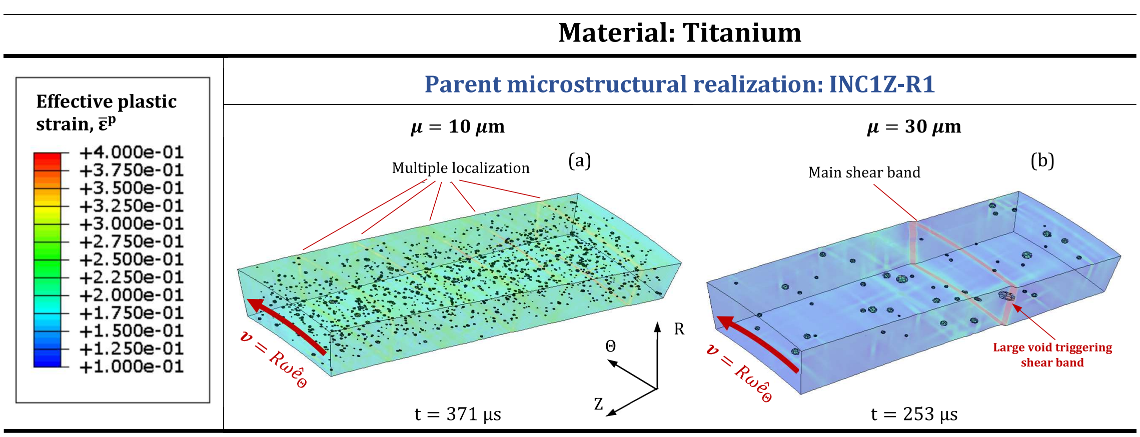

Figure 19: Parent microstructural realization: INC1Z-R1. Material: Titanium. Nominal shear strain rate $\dot{\gamma}_0 = 1000$ s^{-1}. Initial void volume fraction $f_0 = 0.13$ %. Contours of effective plastic strain $\bar{\varepsilon}$ for two different values of the mean voids size: (a) $\mu = 10$ μm and (b) $\mu = 30$ μm.

Fig. 20 shows the shear force F versus the angular displacement ϕ for the distributions with average pore size of $\mu = 16.58$ μm and standard deviations of 18 % and 60 %, which correspond to $dev = 3$ μm and $dev = 10$ μm. These two microstructures contain 464 and 217 pores, respectively. For the microstructure with $dev = 3$ μm, the two largest pores have a diameter of 28.57 μm, the third one of 25.48 μm, and the fourth one of 24.85 μm, i.e., there are small differences in size between the largest pores of the specimen. In contrast, for the microstructure with $dev = 10$ μm, the diameter of the largest void is 61.54 μm, while the second and third larger pores are significantly smaller, 44.56 μm and 44.36 μm, respectively (the differences in the number and the size of the pores between both microstructures are apparent in the isocontours of Fig. 22). Notice that the ductility of the sample with less standard deviation is greater, as smaller pores delay localization. Namely, the critical shear strains for $dev = 3$ μm and $dev = 10$ μm are 0.38 and 0.27, respectively (the reader is referred to Fig. 11b to check the excellent correlation of these results with the fitted curve).

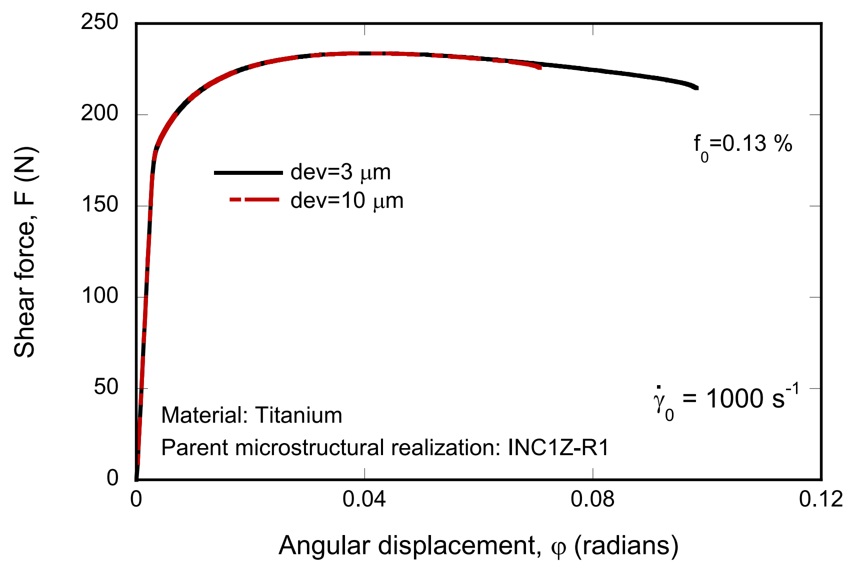

Figure 20: Shear force F versus angular displacement ϕ measured at the *top surface* of the sample indicated in Fig. 1. Material: Titanium. Parent microstructural realization: INC1Z-R1. Nominal shear strain rate $\dot{\gamma}_0 = 1000$ s^{-1}. Results corresponding to two different values of the standard deviation: $dev = 3$ μm and $dev = 10$ μm.

Fig. 21 displays the effective plastic strain $\bar{\varepsilon}^p$ and the local initial void volume fraction f_0^{local} along the normalized axial coordinate $\bar{Z}$ for the void size distributions with standard deviation $dev = 3$ μm –Fig. 21a– and $dev = 10$ μm –Fig. 21b–. Notice that there are more strain peaks for the distribution with smaller standard deviation because the number of voids in the specimen is greater, see Fig. 22, and the difference in size of the voids is less, which favors the formation of multiple localization bands growing at relatively similar speed (the porous microstructure is *more homogeneous*). Namely, the difference between the greatest pore and the tenth greatest pore for $dev = 3$ μm and $dev = 10$ μm is ≈ 8 μm and ≈ 30 μm, respectively. In fact, for the microstructure with

$dev = 3$ μm, none of the ten greatest pores is located at the section of the sample where the main shear band is nucleated, while for $dev = 10$ μm the main shear band is triggered by the greatest void. These results suggest that increasing the standard deviation of the porosity distribution makes the largest voids of the microstructure to have an increasing effect on the localization pattern, which is formed by less localization bands, with the main shear band being triggered by the largest void (which stands out with respect to other pores of the microstructure).

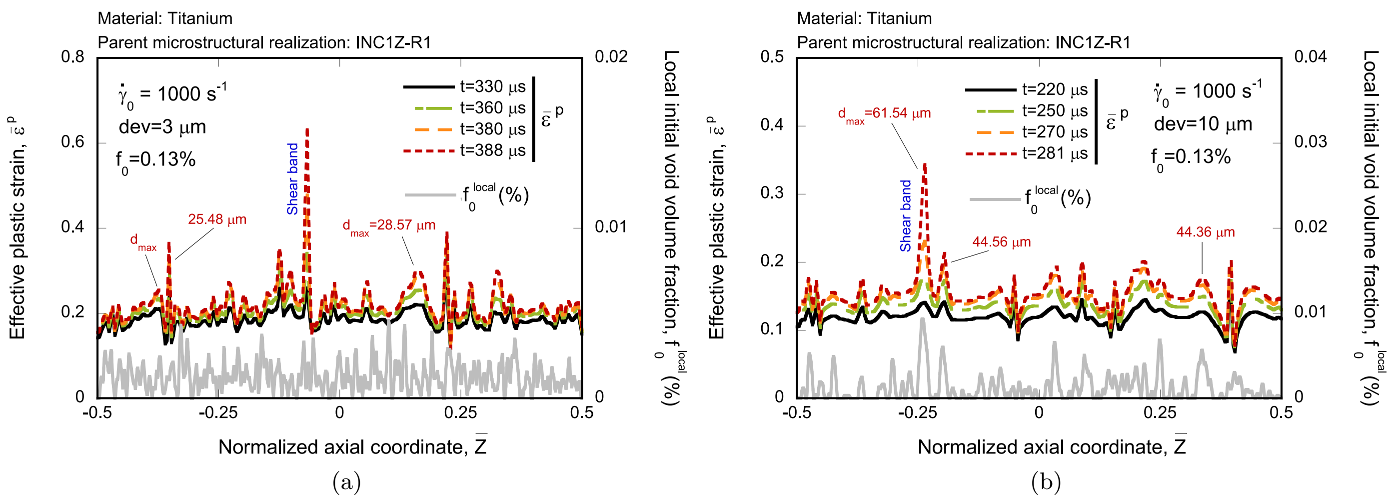

Figure 21: Effective plastic strain $\bar{\varepsilon}^p$ and local initial void volume fraction $f_0^{local}(\%)$ versus normalized axial coordinate $\bar{Z} = \frac{Z}{h}$. The measurement path is referred to as *lateral edge* in Fig. 1. The results for the effective plastic strain correspond to different loading times. Material: Titanium. Parent microstructural realization: INC1Z-R1. Nominal shear strain rate $\dot{\gamma}_0 = 1000$ s^{-1}. Results corresponding to two different values of the standard deviation: (a) $dev = 3$ μm and (b) $dev = 10$ μm.

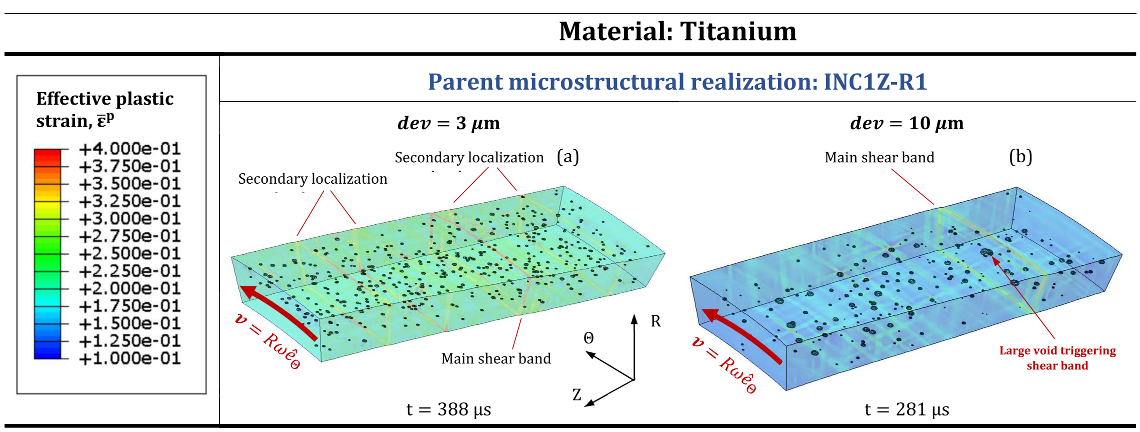

Figure 22: Parent microstructural realization: INC1Z-R1. Material: Titanium. Nominal shear strain rate $\dot{\gamma}_0 = 1000$ s^{-1}. Contours of effective plastic strain $\bar{\varepsilon}$ for two different values of the standard deviation: (a) $dev = 3$ μm and (b) $dev = 10$ μm.

6. Parametric analysis: material effects

The finite element calculations presented in this section correspond to INC1Z-R1. For this microstructure, the diameter of the three larger pores is 62.36 μm, 58.91 μm and 45.11 μm, respectively (see Fig. 8a). The numerical simulations have been carried out for $\dot{\gamma}_0 = 1000$ s^{-1} with baseline parameters corresponding to Titanium (as in Section 5). The effect of thermal softening on shear localization is investigated in Section 6.1 varying the temperature sensitivity exponent of the material, while keeping constant all other parameters included in Table 1. Moreover, Section 6.2 shows calculations performed with different values of the strain rate sensitivity exponent to investigate the influence of material viscosity on the shear band formation.

6.1. The interplay between porous microstructure and thermal softening

Fig. 23 displays the shear force F as a function of the angular displacement ϕ for calculations performed with three different values of the temperature sensitivity exponent: $\nu = 0$, -0.5 and -1 (the three values lead to smaller softening than the reference parameter used in all other calculations reported in this paper for Titanium, see Table 1). For the temperature independent material ($\nu = 0$), the force monotonically increases, preventing the formation of shear bands. In absence of thermal softening, porosity alone does not trigger shear localization (the same conclusion was reached by Vishnu et al. (2022) for the problem of a thick-walled cylinder subjected to dynamic radial collapse). In contrast, the results for $\nu = -0.5$ and -1 show a maximum in the shear force, so that the continuation of the loading process leads to mild plastic localization in the case of $\nu = -0.5$, and intense shear banding for $\nu = -1$.

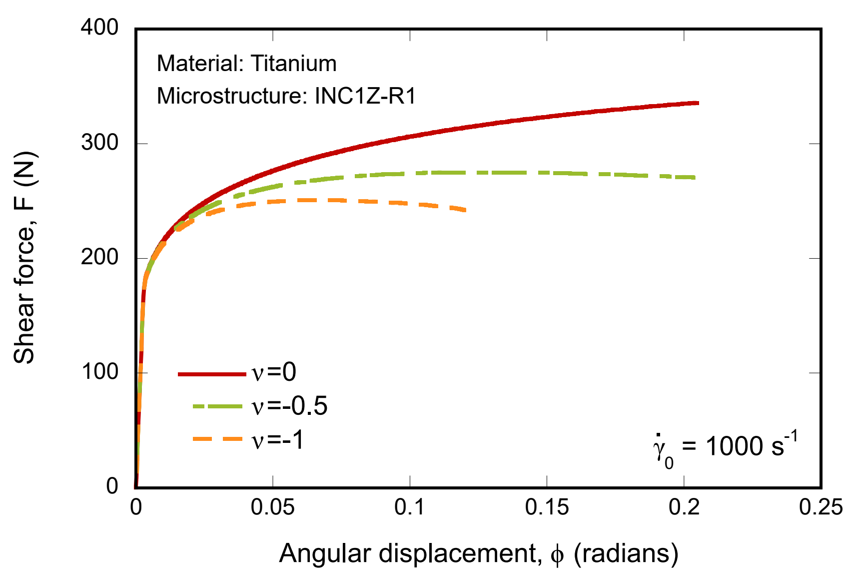

Figure 23: Shear force F versus angular displacement ϕ measured at the *top surface* of the sample indicated in Fig. 1. Material: Titanium. Microstructure: INC1Z-R1. Nominal shear strain rate $\dot{\gamma}_0 = 1000$ s^{-1}. Results corresponding to three different values of the temperature sensitivity exponent: $\nu = 0$ (temperature independent material), $\nu = -0.5$ and $\nu = -1$.

Fig. 24 shows the evolution of the effective plastic strain $\bar{\varepsilon}^p$ and the local initial void volume fraction f_0^{local} versus the normalized axial coordinate $\bar{Z}$ for the three values of the temperature sensitivity exponent considered. For the temperature independent material, the effective plastic strain is largely constant along the sample, the porous microstructure deforming during loading, creating concentrations of strain that do not lead to shear banding (eventually, the simulation stops due to excessive distortion of the elements surrounding the voids). For $\nu = -0.5$, the $\bar{\varepsilon}^p - \bar{Z}$ curves display several excursions of strain which correspond to incipient localization bands, while the calculation for $\nu = -1$ develops a localization pattern with a main shear band and several secondary localizations. Notice that the localization pattern is the same obtained in Fig. 8a for the reference value of the temperature sensitivity exponent, but less developed because the thermal softening is less pronounced. The main shear band is triggered by the cluster formed by the second and third largest pores of the microstructure, which are located nearly at the same section of the sample. The largest pore of the microstructure is responsible for the secondary localization located at $\bar{Z} = 0.2$.

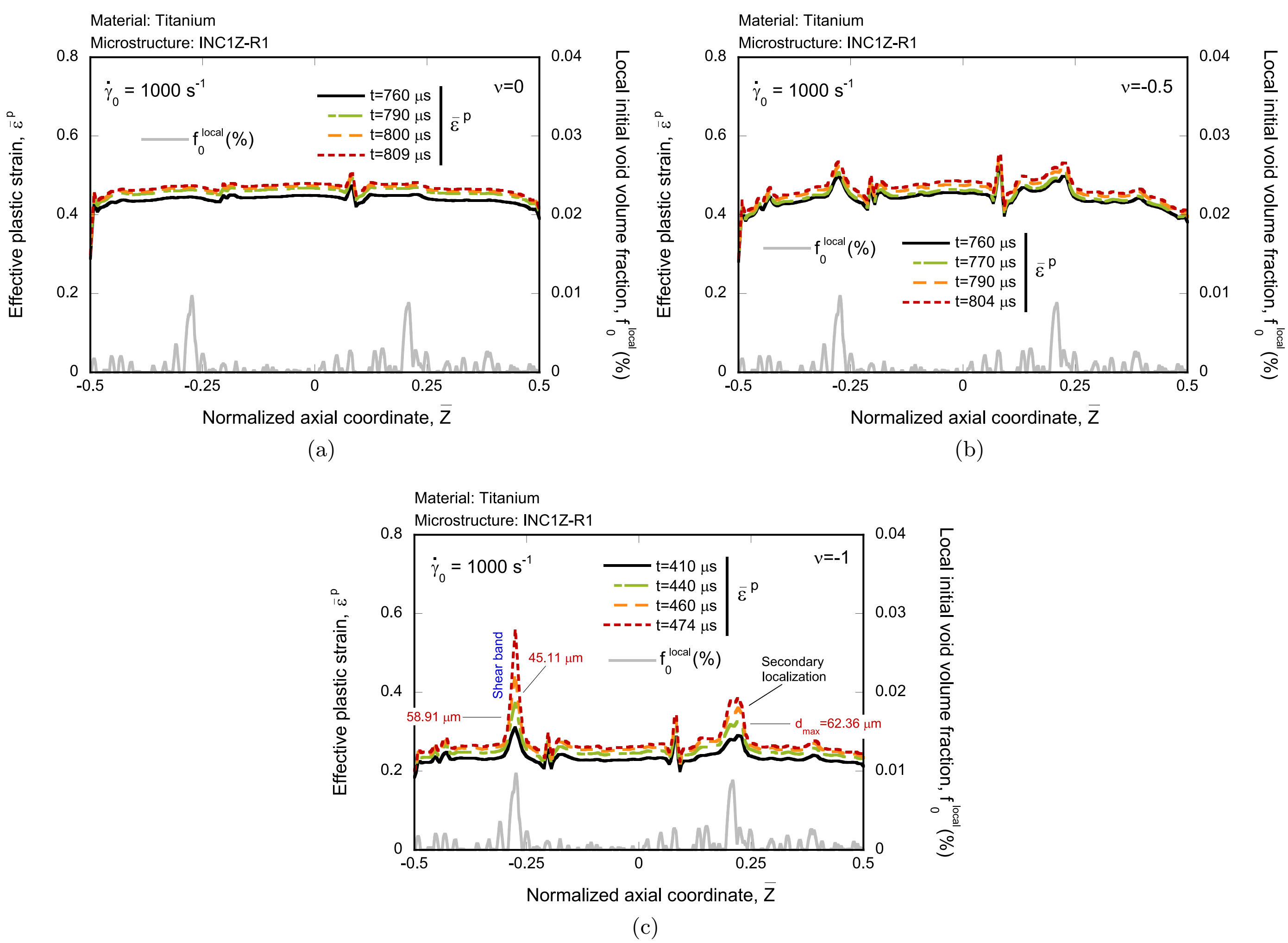

Figure 24: Effective plastic strain $\bar{\varepsilon}^p$ and local initial void volume fraction $f_0^{local}(\%)$ versus normalized axial coordinate $\bar{Z} = \frac{Z}{h}$. The measurement path is referred to as *lateral edge* in Fig. 1. The results for the effective plastic strain correspond to different loading times. Material: Titanium. Microstructure INC1Z-R1. Nominal shear strain rate $\dot{\gamma}_0 = 1000$ s^{-1}. Results corresponding to three different values of the temperature sensitivity exponent: (a) $\nu = 0$ (temperature independent material), (b) $\nu = -0.5$ and (c) $\nu = -1$.

6.2. The interplay between porous microstructure and strain rate sensitivity

Fig. 25 shows the shear force versus the angular displacement for calculations performed with two different strain rate sensitivity exponents, $m = 0.05$ and $m = 0.1$ (the two values are greater than the reference parameter used in all other calculations reported in this paper for Titanium, see Table 1). Increasing the value of m shifts upwards the $F - \phi$ curve and moves to lower angular displacement the maximum value of the force, leading to more pronounced softening. Still, the loss of load carrying capacity for $m = 0.1$ occurs for greater value of the angular displacement, so that the critical shear strains computed for $m = 0.05$ and $m = 0.1$ are 0.31 and 0.37, respectively. These results make apparent the stabilizing effect of strain rate sensitivity on material behavior, which delays shear localization (see also Shawki and Clifton (1989) and Molinari (1991)).

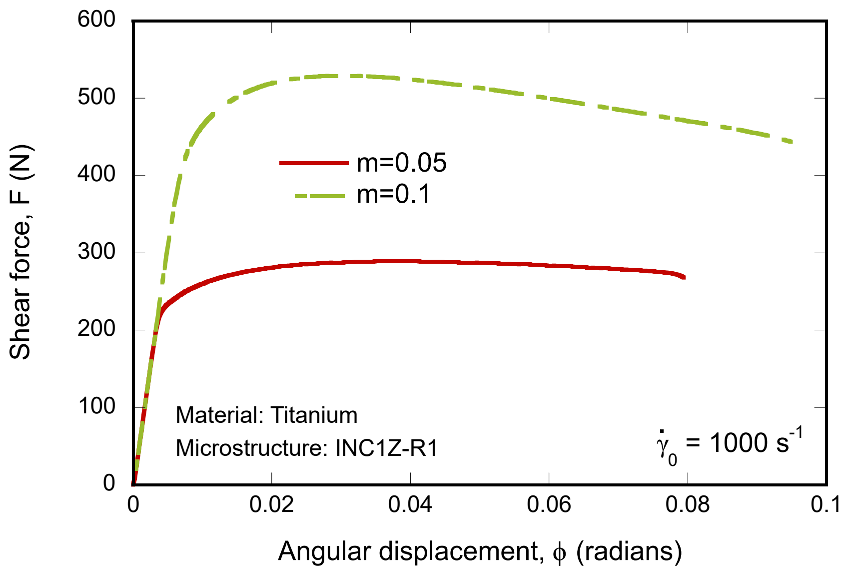

Figure 25: Shear force F versus angular displacement ϕ measured at the *top surface* of the sample indicated in Fig. 1. Material: Titanium. Microstructure: INC1Z-R1. Nominal shear strain rate $\dot{\gamma}_0 = 1000\ \mathrm{s}^{-1}$. Results corresponding to two different values of the strain rate sensitivity exponent: $m = 0.05$ and $m = 0.1$.

The effect of the material strain rate sensitivity on the shear localization process is further illustrated in Fig. 26, which shows the evolution along the normalized axial coordinate of the effective plastic strain and the local initial void volume fraction for $m = 0.05$ and $m = 0.1$. The morphology of the localization pattern is the same for both strain rate sensitivity exponents, with the main shear band located at $\bar{Z} = -0.27$, at the section of the sample where the second and third largest pores of the microstructure are located (see Section 6.1). On the other hand, the main shear band is less developed with the increase of m, because the strain rate sensitivity slows down plastic localization.

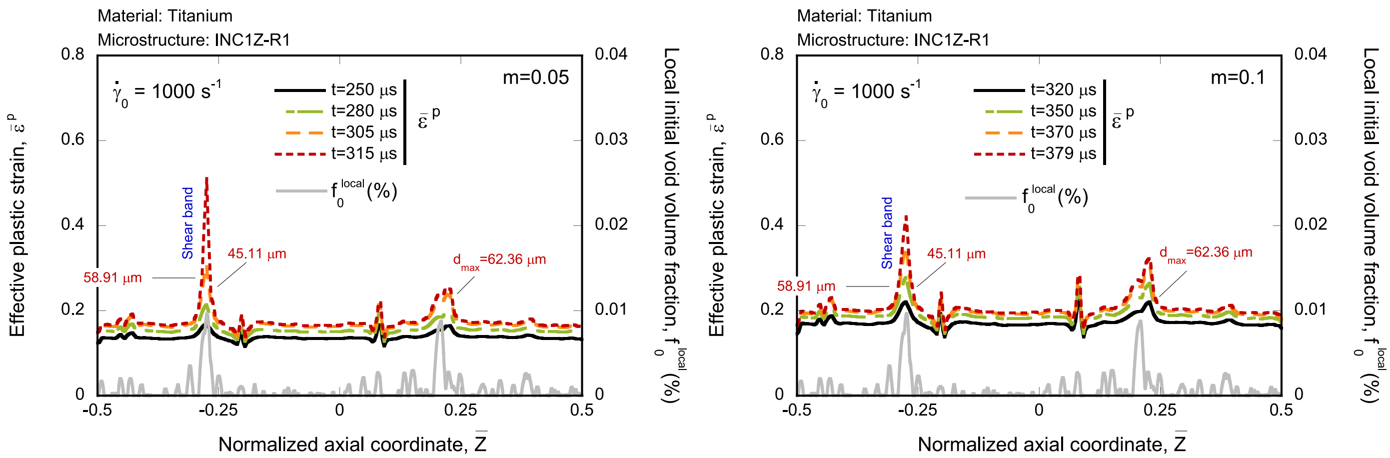

(a) (b)

Figure 26: Effective plastic strain $\bar{\varepsilon}^p$ and local initial void volume fraction $f_0^{local}(\%)$ versus normalized axial coordinate $\bar{Z} = \frac{Z}{h}$. The measurement path is referred to as *lateral edge* in Fig. 1. The results for the effective plastic strain correspond to different loading times. Material: Titanium. Microstructure: INC1Z-R1. Nominal shear strain rate $\dot{\gamma}_0 = 1000\ \mathrm{s}^{-1}$. Results corresponding to two different values of the strain rate sensitivity parameter: (a) $m = 0.05$ and (b) $m = 0.1$.

7. Parametric analysis: loading rate effects

The finite element calculations presented in this section correspond to INC1Z-R1 (the same microstructure considered in Section 6), and have been performed with material parameters corresponding to Titanium (as in Section 5). Three shear strain rates have been investigated, $\dot{\gamma}_0 = 100\ \mathrm{s}^{-1}$, $5000\ \mathrm{s}^{-1}$ and $10000\ \mathrm{s}^{-1}$. This range of strain rates encompasses the maximum and minimum strain rates used in dynamic torsion experiments, see Section 1.

Fig. 27 shows the evolution of the shear force with the angular displacement. Increasing the value of $\dot{\gamma}_0$ shifts the $F - \phi$ curve upwards –due to the strain rate sensitivity of the material–, which in turn increases the thermal softening, leading to earlier loss of load carrying capacity. These results suggest that, for the problem addressed in this paper, and the range of strain rates considered, the effect of inertia seems to be small (or negligible), as no stabilizing effect on the material behavior is observed with the increase of the strain rate. The critical shear strains obtained for $\dot{\gamma}_0 = 100\ \mathrm{s}^{-1}$, $5000\ \mathrm{s}^{-1}$ and $10000\ \mathrm{s}^{-1}$, are $\gamma_c = 0.28$, 0.26 and 0.25, respectively. The fact that the role of inertia seems to be small (or negligible), is consistent with the evidence that the localization process and the specimen ductility are largely controlled by the larger pores of the microstructure (see Fig. 11b).

The comparison of the localization patterns that develop in the specimen for $\dot{\gamma}_0 = 100\ \mathrm{s}^{-1}$ and $10000\ \mathrm{s}^{-1}$, see Fig. 28, makes apparent that, for the loading rates investigated, the location of the main shear band and of the secondary localizations is independent of the strain rate (i.e., independent of inertia effects). While the same

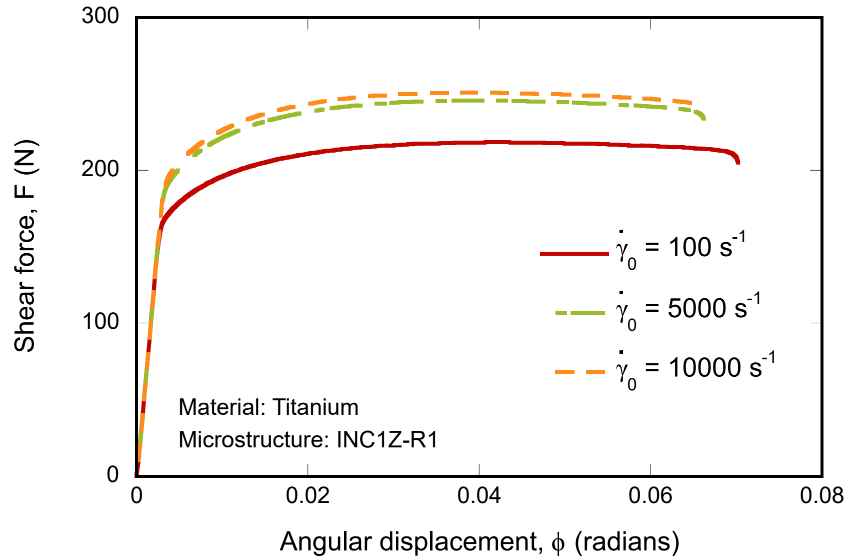

Figure 27: Shear force F versus angular displacement ϕ measured at the *top surface* of the sample indicated in Fig. 1. Material: Titanium. Microstructure INC1Z-R1. Results corresponding to three different values of the nominal shear strain rate: $\dot{\gamma}_0 = 100$ s^{-1}, $\dot{\gamma}_0 = 5000$ s^{-1} and $\dot{\gamma}_0 = 10000$ s^{-1}.

conclusions are obtained for other microstructures, such results are not shown for the sake of brevity.

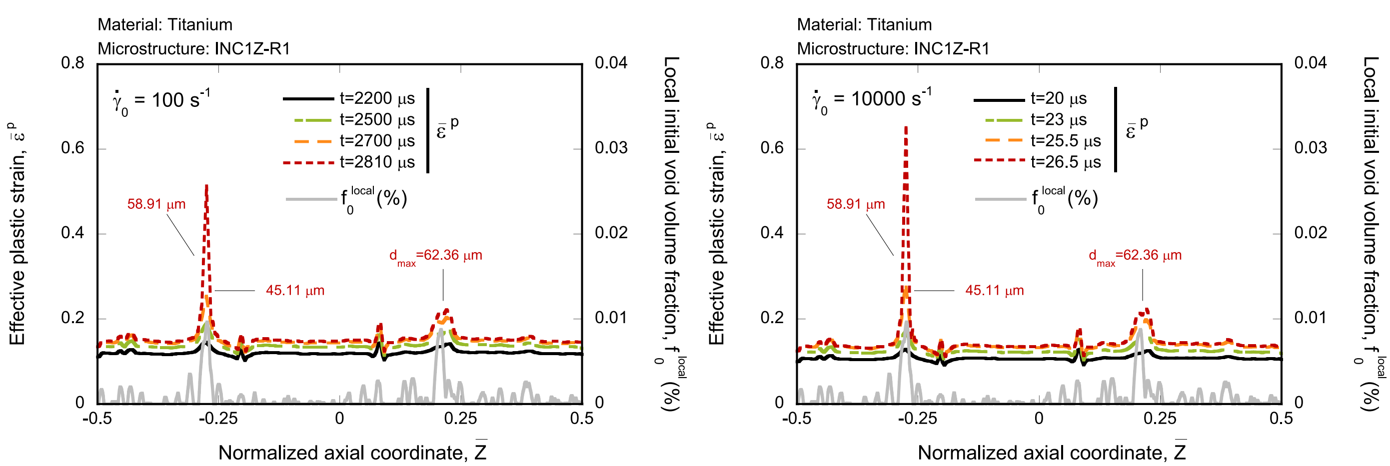

(a) (b)

Figure 28: Effective plastic strain $\bar{\varepsilon}^p$ and local initial void volume fraction $f_0^{local}(\%)$ versus normalized axial coordinate $\bar{Z} = \frac{Z}{h}$. The measurement path is referred to as *lateral edge* in Fig. 1. The results for the effective plastic strain correspond to different loading times. Material: Titanium. Microstructure INC1Z-R1. Results corresponding to three different values of the nominal shear strain rate: (a) $\dot{\gamma}_0 = 100$ s^{-1} and (c) $\dot{\gamma}_0 = 10000$ s^{-1}.

8. Concluding remarks

In this paper, we have performed numerical calculations of thin-walled tubes subjected to dynamic twisting to study the effect of material porosity on adiabatic shear banding under simple shear loading. The novelty is that the finite element models developed include explicitly resolved pores randomly distributed in the sample, so that the distributions of void sizes investigated are representative of four different additive manufactured metals in which the initial void volume fraction varies from ≈ 0.001 % to ≈ 2 %, and the voids size between ≈ 6 μm and ≈ 110 μm. All previous works simulating dynamic torsion of porous tubes have employed standard homogenized constitutive models based on *ad-hoc* definitions of the void shearing/softening mechanisms, in which the porosity stands for a single damage parameter with no contribution of the spatial variation and size distribution of voids. The alternative approach presented in this work has led to the following conclusions:

- The spatial distribution of voids affects the morphology of the shear localization pattern, as the main shear band is generally nucleated at the location of the largest pore of the microstructure.
- The size distribution of voids affects the morphology of the shear localization pattern such that when the pores show large differences in size, the main shear band stands out over the secondary localizations.
- The number of voids affects the morphology of the shear localization pattern such that as the number of voids increases, more secondary localizations are nucleated.
- The maximum voids size is the main feature of the porous microstructure affecting the specimen ductility, over and above the void volume fraction.
- For a given set of material parameters, it is possible to obtain a master curve which determines the decrease of the sample ductility with the size of the largest pore of the microstructure.
- Neither the loading rate, nor the strain rate sensitivity of the material affect the morphology of the shear localization pattern, which is largely controlled by the porous microstructure.
- Increasing the strain rate sensitivity of the material leads to increasing strain softening, yet the stabilizing effect of viscosity delays the formation of the localization pattern and increases specimen ductility.
- The porous microstructure alone does not lead to strain softening, showing that the contribution of adiabatic heating is needed for the shear localization pattern to form.
- For the loading rates considered, the effect of inertia is virtually negligible, as specimen ductility slightly decreases with the increase of the strain rate.

While these conclusions are consistent with the results presented by Vishnu et al. (2022) for the problem of a porous thick-walled cylinder subjected to rapid radial collapse, the calculations presented in this paper have the advantages that (i) the stress state is simple shear and (ii) only one main shear band is generally formed, which facilitates the interpretation of results and future experimental verification (since torsional split Hopkinson bar tests are relatively standard experiments, as compared to the collapse thick-walled cylinders using electromagnetic forces or explosions).

Funding

The research leading to these results has received funding from the European Research Council (ERC) under the European Union's Horizon 2020 research and innovation programme. Project PURPOSE, grant agreement 758056.

J. C. Nieto-Fuentes acknowledges support from the CONEX-Plus programme funded by Universidad Carlos III de Madrid and the European Union's Horizon 2020 research and innovation programme, under the Marie Skłodowska-Curie grant agreement 801538.

Conflict of interest

The authors declare that they have no conflict of interest.

Author contributions

A. R. Vishnu: Conceptualization; Data curation; Formal analysis; Investigation; Software; Validation; Writing - original draft; Writing - review & editing. **J. C. Nieto-Fuentes**: Investigation; Methodology; Supervision; Writing - review & editing. **J. A. Rodríguez-Martínez**: Conceptualization; Formal analysis; Funding acquisition; Investigation; Methodology; Project administration; Resources; Supervision; Validation; Visualization; Writing - original draft; Writing - review & editing.

References

ABAQUS/Standard, 2019. Abaqus Standard v6.16 User's Manual. version 6.16 ed., ABAQUS Inc., Richmond, USA.

Arriaga, M., Waisman, H., 2017. Combined stability analysis of phase-field dynamic fracture and shear band localization. International Journal of Plasticity 96, 81–119.

Bai, Y., Xuc, Q., Xu, Y., Shen, L., 1994. Characteristics and microstructure in the evolution of shear localization in Ti-6A1-4V alloy. Mechanics of Materials 17, 155–64.

Batra, R., Kim, C., 1990. Effect of viscoplastic flow rules on the initiation and growth of shear bands at high strain rates. Journal of the Mechanics and Physics of Solids 38, 859–74.

Batra, R., Kim, C., 1991. Effect of thermal conductivity on the initiation, growth and bandwidth of adiabatic shear bands. International Journal of Engineering Science 29, 949–60.

Batra, R., Kim, C., 1992. Analysis of shear banding in twelve materials. International Journal of Plasticity 8, 425–52.

Batra, R.C., Zhang, X., 1994. On the propagation of a shear band in a steel tube. Journal of Engineering Materials and Technology 116, 155–61.

Bonnet-Lebouvier, A.S., Molinari, A., Lipinski, P., 2002. Analysis of the dynamic propagation of adiabatic shear bands. International Journal of Solids and Structures 39, 4249–69.

Børvik, T., Leinum, J.R., Solberg, J.K., Hopperstad, O.S., Langseth, M., 2001. Observations on shear plug formation in Weldox 460 E steel plates impacted by blunt-nosed projectiles. International Journal of Impact Engineering 25, 553–72.

Burns, T.J., Davies, M.A., 2002. On repeated adiabatic shear band formation during high-speed machining. International Journal of Plasticity 18, 487–506.

Chichili, D.R., Ramesh, K., Hemker, K.J., 2004. Adiabatic shear localization in α-titanium: experiments, modeling and microstructural evolution. Journal of the Mechanics and Physics of Solids 52, 1889–909.

Cho, K., Chi, Y., Duffy, J., 1990. Microscopic observations of adiabatic shear bands in three different steels. Metallurgical Transactions A 21, 1161–75.

Cho, K.M., Lee, S., Nutt, S., Duffy, J., 1993. Adiabatic shear band formation during dynamic torsional deformation of an hy-100 steel. Acta Metallurgica et Materialia 41, 923–32.

Da Silva, M., Ramesh, K., 1997. The rate-dependent deformation and localization of fully dense and porous ti-6al-4v. Materials Science and Engineering: A 232, 11–22.

Dodd, B., Atkins, A.G., 1983. Flow localization in shear deformation of void-containing and void-free solids. Acta Metallurgica 31, 9–15.

Dodd, B., Bai, Y., 1985. Width of adiabatic shear bands. Materials Science and Technology 1, 38–40.

Dodd, B., Bai, Y., 2012. Adiabatic shear localization: frontiers and advances. Elsevier.

Dolinski, M., Rittel, D., Dorogoy, A., 2010. Modeling adiabatic shear failure from energy considerations. Journal of the Mechanics and Physics of Solids 58, 1759–75.

Dorothy, H.L., Longère, P., 2019. Unified modelling of adiabatic shear banding and subsequent micro-voiding driven dynamic failure of viscoplastic solids. International Journal of Impact Engineering 132, 103322.

Duffy, J., Chi, Y., 1992. On the measurement of local strain and temperature during the formation of adiabatic shear bands. Materials Science and Engineering: A 157, 195–210.

Feng, H., Bassim, M., 1999. Finite element modeling of the formation of adiabatic shear bands in AISI 4340 steel. Materials Science and Engineering: A 266, 255–60.

Gaudillière, C., Ranc, N., Larue, A., Lorong, P., 2010. Investigations in high speed blanking: cutting forces and microscopic observations. EPJ Web of Conferences 6.

Giovanola, J.H., 1988a. Adiabatic shear banding under pure shear loading. Part I: direct observation of strain localization and energy dissipation measurements. Mechanics of Materials 7, 59–71.

Giovanola, J.H., 1988b. Adiabatic shear banding under pure shear loading. Part II: fractographic and metallographic observations. Mechanics of Materials 7, 73–87.

Glema, A., Łodygowski, T., Perzyna, P., 2008. Numerical investigation of dynamic shear bands in inelastic solids as a problem of mesomechanics. Computational Mechanics 41, 219–29.

Gurson, A.L., 1977. Continuum theory of ductile rupture by void nucleation and growth. Part I: Yield criteria and flow rules for porous ductile media. ASME Journal of Engineering Materials and Technology 99, 2–15.

Hartley, K., Duffy, J., Hawley, R., 1987. Measurement of the temperature profile during shear band formation in steels deforming at high strain rates. Journal of the Mechanics and Physics of Solids 35, 283–301.

Johnson, G.R., 1981. Dynamic Analysis of a Torsion Test Specimen Including Heat Conduction and Plastic Flow. Journal of Engineering Materials and Technology 103, 201–6.

Johnson, G.R., Hoegfeldt, J.M., Lindholm, U.S., Nagy, A., 1983. Response of Various Metals to Large Torsional Strains Over a Large Range of Strain Rates—Part 1: Ductile Metals. Journal of Engineering Materials and Technology 105, 42–7.

Kobayashi, H., Dodd, B., 1989. A numerical analysis for the formation of adiabatic shear bands including void nucleation and growth. International Journal of Impact Engineering 8, 1–13.

Kubair, D., Ramesh, K., Swaminathan, P., 2015. Effect of shear-void-growth-softening on adiabatic shear-band-spacing in ductile materials. Acta Mechanica 226, 4189–206.

Łodygowski, T., Perzyna, P., 1997a. Localized fracture in inelastic polycrystalline solids under dynamic loading processes. International Journal of Damage Mechanics 6, 364–407.

Łodygowski, T., Perzyna, P., 1997b. Numerical modelling of localized fracture of inelastic solids in dynamic loading processes. International Journal for Numerical Methods in Engineering 40, 4137–58.

Lovinger, Z., Rittel, D., Rosenberg, Z., 2015. An experimental study on spontaneous adiabatic shear band formation in electro-magnetically collapsing cylinders. Journal of the Mechanics and Physics of Solids 79, 134–56.

Marchand, A., Duffy, J., 1988. An experimental study of the formation process of adiabatic shear bands in a structural steel. Journal of the Mechanics and Physics of Solids 36, 251–83.

Marvi-Mashhadi, M., Vaz-Romero, A., Sket, F., Rodríguez-Martínez, J.A., 2021. Finite element analysis to determine the role of porosity in dynamic localization and fragmentation: Application to porous microstructures obtained from additively manufactured materials. International Journal of Plasticity 143, 102999.

Mgbokwere, C., Nutt, S., Duffy, J., 1994. Shear band formation in 4340 steel: A tem study. Mechanics of Materials 17, 97–110.

Mises, R.V., 1928. Mechanik der plastischen formänderung von kristallen. ZAMM - Journal of Applied Mathematics and Mechanics / Zeitschrift für Angewandte Mathematik und Mechanik 8, 161–85.

Molinari, A., 1991. Shear band analysis, in: Non Linear Phenomena in Materials Science I, Trans Tech Publications Ltd. pp. 447–67.

Molinari, A., 1997. Collective behaviour and spacing of adiabatic shear bands. Journal of the Mechanics and Physics of Solids 45, 1551–75.

Molinari, A., Clifton, R., 1987. Analytical characterization of shear localization in themoviscoplastic materials. Journal of Applied Mechanics 54, 806–12.

Molinari, A., Musquar, C., Sutter, G., 2002. Adiabatic shear banding in high speed machining of Ti-6Al-4V: Experiments and modeling. International Journal of Plasticity 18, 443–59.

Nahshon, K., Hutchinson, J., 2008. Modification of the gurson model for shear failure. European Journal of Mechanics-A/Solids 27, 1–17.

Needleman, A., 1991. The effect of material inertia on neck development. In: Yang, W.H. (Ed.), Topics in Plasticity. AM Press, Ann Arbor, MI , 151–60.

Odeshi, A.G., Al-Ameeri, S., Mirfakhraei, S., Yazdani, F., Bassim, M.N., 2006. Deformation and failure mechanism in AISI 4340 steel under ballistic impact. Theoretical and Applied Fracture Mechanics 45, 18–24.

Pascon, J.P., Waisman, H., 2021. A thermodynamic framework to predict ductile damage in thermoviscoplastic porous metals. Mechanics of Materials 153, 103701.

Perzyna, P., 1994. Adiabatic shear band localization fracture of solids in dynamic loading processes. Le Journal de Physique IV 4, C8–441.

Ramesh, K., 1994. On the localization of shearing deformations in tungsten heavy alloys. Mechanics of Materials 17, 165–73.

Schmitz, F., Winter, S., Clausmeyer, T., Wagner, M.F.X., Tekkaya, A.E., 2020. Adiabatic blanking of advanced high-strength steels. CIRP Annals 69, 269–72.

Shawki, T.G., Clifton, R.J., 1989. Shear band formation in thermal viscoplastic materials. Mechanics of Materials 8, 13–43.

Vishnu, A.R., Marvi-Mashhadi, M., Nieto-Fuentes, J.C., Rodríguez-Martínez, J.A., 2022. New insights into the role of porous microstructure on dynamic shear localization. International Journal of Plasticity , 103150.

Wiehahn, M.A., Nurick, G.N., Bowles, H.C., 2000. Some insights into the mechanism of the deformation and tearing of thin plates at high strain rates incorporating temperature dependent material properties. WIT Transactions on the Built Environment 48.

Xue, Q., Meyers, M.A., Nesterenko, V.F., 2002. Self-organization of shear bands in titanium and Ti–6Al–4V alloy. Acta materialia 50, 575–96.

Xue, Z., Vaziri, A., Hutchinson, J.W., 2008. Material aspects of dynamic neck retardation. Journal of the Mechanics and Physics of Solids 56, 93–113.

Yang, Y., Zheng, H.G., Zhao, Z.D., Zhang, Q., Zhang, Q.M., Jiang, F., Li, X.M., 2011. Effect of phase composition on self-organization of shear bands in Ti-1300 titanium alloy. Materials Science and Engineering: A 528, 7506–13.

Ye, G.G., Xue, S.F., Jiang, M.Q., Tong, X.H., Dai, L.H., 2013. Modeling periodic adiabatic shear band evolution during high speed machining Ti-6Al-4V alloy. International Journal of Plasticity 40, 39–55.

Zener, C., Hollomon, J.H., 1944. Effect of strain rate upon plastic flow of steel. Journal of Applied Physics 15, 22–32.

Zou, D.L., Zhen, L., Xu, C.Y., Shao, W.Z., 2011. Characterization of adiabatic shear bands in AM60B magnesium alloy under ballistic impact. Materials characterization 62, 496–502.